Title

Local reciprocal release of GABA from olfactory bulb granule cell spines: Cooperation of conventional release mechanisms and NMDA receptors

Authors

Vanessa Lage-Rupprecht[1,2], Li Zhou[1], Gaia Bianchini[1], S. Sara Aghvami[1,3,4], Balázs Rózsa[5], Marco Sassoé-Pognetto[6] & Veronica Egger[1*]

Affiliations

1. Neurophysiology, Institute of Zoology, Universität Regensburg, 93040 Regensburg, Germany; 2. Fraunhofer SCAI, 53754 Sankt Augustin, Germany; 3. School of Electrical and Computer Engineering, University of Tehran, 14395-515 Tehran, Iran; 4. School of Cognitive Sciences, Institute for Research in Fundamental Sciences (IPM), 19395-5746 Tehran, Iran; 5. Two-Photon Imaging Center, Institute of Experimental Medicine, Hungarian Academy of Sciences, 1039 Budapest, Hungary; 6. Neuroscience Department, University of Turin, I-10126 Torino, Italy.

15 ***Abstract***

16 In the rodent olfactory bulb the smooth dendrites of the principal glutamatergic mitral cells
17 (MCs) engage in reciprocal dendrodendritic interactions with the large spines of GABAergic
18 granule cells (GC), where unitary release of glutamate gives rise to a postsynaptic local
19 activation of voltage-gated Na^+ channels (Na_v), i.e. a spine spike. Can single MC inputs thus
20 trigger reciprocal release? Here we show that unitary-like activation via two-photon uncaging
21 of glutamate causes GC spines to release GABA both synchronously and asynchronously
22 onto MC dendrites, detected as IPSCs at the MC soma. This release indeed requires
23 activation of Na_v and high-voltage-activated Ca^{2+} channels (HVACCs), but also NMDA
24 receptor (NMDAR) activation. Simulations show a substantial temporal overlap of HVACC-
25 and NMDAR-mediated Ca^{2+} currents during the spine spike, and ultrastructural data prove
26 NMDAR presence within the GABAergic presynapse. Thus output from the GC spine
27 reciprocal microcircuit relies on cooperative action of HVACCs and presynaptic NMDARs.

28 ***Introduction***

29 Reciprocal dendrodendritic microcircuits can be found in several parts of the nervous system
30 and are especially abundant in the vertebrate olfactory bulb (Crespo et al., 2013), where the
31 dendrites of the principal mitral and tufted cells (MTCs) engage in such interactions with at
32 least three major subtypes of local GABAergic neurons, namely periglomerular cells in the
33 glomerular layer, and parvalbumin and granule cells (GC) in the external plexiform layer. The
34 latter synapse differs from the other bulbar reciprocal arrangements by its location within a
35 large spine on the GC side. These spines feature particularly long necks (Woolf et al., 1991)
36 which might serve to electrically isolate the synapse and boost local processing (e.g. Miller et
37 al., 1985; Spruston, 2008). Indeed, we have gathered evidence that postsynaptic potentials
38 in GC spines are electrically compartmentalized and thus can locally activate voltage-gated
39 Na channels (Na_v) which in turn activate classic presynaptic N/P/Q Ca^{2+} channels within the
40 spine ('spine spike', Bywalez et al., 2015). These observations reinforce our earlier notion of
41 the reciprocal spine as a mini-neuron that is predicted to generate synaptic output upon local
42 activation (Egger and Urban, 2006).

43 While there have been many earlier studies of recurrent dendrodendritic inhibition (DDI) at
44 the MTC-GC synapse, it is unknown whether a unitary, purely local activation of the spine's

microcircuit can indeed trigger release of GABA back onto the exciting MTC. The issue is still unresolved because (1) paired recordings of synaptically coupled GCs and MTCs are notoriously hard to perform (e.g. Pressler and Strowbridge, 2017) and would also not allow to fully dissect the circuit, and (2) most of these earlier studies used a strong stimulation of voltage-clamped MCs, namely a depolarization to 0 mV for 20-50 ms (Isaacson and Strowbridge, 1998; Halabisky et al., 2000; Isaacson, 2001; Chen et al., 2000). This DDI protocol is likely to cause a massive release of glutamate from the lateral MC dendrites and was indeed shown to invoke glutamate spillover between them (Isaacson, 1999). It results in long-lasting recurrent inhibition with both synchronous and asynchronous components, the latter with a time constant of ~ 500 ms. For this type of DDI, NMDA receptor (NMDAR) activation was shown to be an important source of Ca^{2+} entry that suffices to trigger release of GABA from the GC spine under conditions of zero extracellular $[Mg^{2+}]_e$ (also in Schoppa et al. 1998). However, such a strong role of NMDARs has been subject to debate, and under conditions of normal $[Mg^{2+}]_e$ it was found that DDI-evoked release from GC spines is mostly abolished by HVACC blockade (Isaacson, 2001; see Discussion).

The MC lateral dendrites are densely covered with GABAergic synapses (Bartel et al., 2015; Sailor et al., 2016). These inputs become strongly attenuated with distance from the MC soma (λ ~ 80 µm, Lowe, 2002), but are probably capable of shunting propagating APs at any point along the dendrite (Lowe, 2002; Xiong et al., 2002). While proximal inputs are thought to be mostly mediated by GC spines, recent studies have revealed reciprocal dendrodendritic interactions also with other GABAergic cell types such as SOM+ neurons, CRH+ neurons and most prominently parvalbumin/PV+ neurons that all feature aspiny, smooth dendrites (partially overlapping populations; Toida et al., 1994; Lepousez et al., 2010; Huang et al., 2013; Kato et al., 2013; Miyamichi et al., 2013). Aside from postsynaptic $GABA_A$Rs, MC lateral dendrites bear scattered NMDA autoreceptors (Sassoé-Pognetto et al., 2003), and AMPA autoreceptors have been detected in the apical tuft and at the soma, giving rise to both autoexcitation and spillover effects (e.g. Aroniadou-Anderjaska et al., 1999; Isaacson, 1999; Friedman and Strowbridge, 2000; Didier et al., 2001; Salin et al., 2001).

73 Here we aim to determine whether – and possibly how - single inputs from MC lateral
74 dendrites to GC spines can also trigger recurrent release of GABA from the reciprocal
75 synapse, using recordings from labeled MCs and two-photon uncaging (TPU) of glutamate
76 along their lateral dendrite near a Venus-tagged GC spine. The mini-neuron hypothesis
77 along with the GC spine spike phenomenon suggest that just like in conventional axons, Na_v
78 channel and ensuing HVACC activation are required to cause release.
79
80 ***Results***
81 *Experimental configuration*
82 To enable pharmacological interference with components of the reciprocal microcircuit such
83 as Na_vs and HVACCs, we bypassed release from the MC presynapse via TPU of DNI-caged
84 glutamate (DNI, see Methods; Chiovini et al., 2014; Bywalez et al., 2015; Palfi et al. 2018) in
85 acute juvenile rat olfactory bulb slices, while recording from MCs in somatic whole-cell
86 voltage-clamp. To visualize the lateral dendrites, MCs were filled with the dye Alexa594 (50
87 μM). Fig. 1A shows the recording configuration.
88 In all MC recordings we observed a high basal frequency of spontaneous events which is a
89 general hallmark of the olfactory bulb network (Egger and Urban, 2006). Wash-in of 1 mM
90 DNI further increased the basal frequency by on average 1.9 ± 1.2 times (mean value before
91 DNI: 4.5 ± 2.1 Hz, n = 14, $P < 0.01$), due to the disinhibition resulting from a partial blockade
92 of $GABA_A$Rs by DNI, which also reduced the mean spontaneous IPSC amplitude to a fraction
93 of 0.47 ± 0.16 of control (n = 14 MCs, $P < 0.001$, Fig. S1A,B,C). In the presence of DNI, the
94 $GABA_A$R antagonist bicuculline (BCC, 50 μM) blocked spontaneous activity almost
95 completely (frequency: 0.13 ± 0.10 of control, n = 6, $P < 0.01$, Fig. 1C, Fig. S1A).
96 Since in initial experiments we occasionally observed activation of both NMDA and AMPA
97 autoreceptors on MC dendrites at a holding potential of -70 mV, MCs were clamped to +10
98 mV in the main body of experiments, near the reversal potential of ionotropic glutamate
99 receptors (Isaacson, 1999; Friedman and Strowbridge, 2000). All experiments were
100 performed at physiological levels of $[Mg^{2+}]_e$ (1 mM).
101 *Triggering of reciprocal IPSCs via TPU*

102 To prevent overstimulation with glutamate, we uncaged with similar laser parameter settings
103 as in the previous study (Bywalez et al., 2015), in which TPU-evoked GC Ca^{2+} signals were
104 indistinguishable from those of unitary spontaneous or triggered synaptic inputs, and
105 routinely tested these settings (see Methods). In most experiments, uncaging was performed
106 at one spot in the immediate vicinity of GC spines that were visible in VGAT-Venus rats and
107 in close proximity (0.2 – 0.5 µm) to the MC lateral dendrite (e.g. Fig. 1A, 2A); in a few initial
108 experiments in WT rats uncaging was performed 'blindly' at up to four spots along the
109 dendrite (to increase the likelihood for triggering a unitary response, e.g. Fig. 2B, see
110 Methods). Responses were detectable in ~ 30% of tested MCs (total n = 166, see Methods).
111 All uncaging spots were located proximally, at distances < 50 µm from the MC soma (Suppl.
112 Fig. S1D). The rationale for this choice was twofold. First we aimed to minimize electrotonic
113 attenuation, since IPSC amplitudes were small (see above, Suppl. Fig. S1). Second, GC
114 inputs are located more proximally as compared to the widely distributed PV+ neuron inputs
115 (Kato et al., 2013; Miyamichi et al., 2013). In addition, PV+ neuron dendrites are smooth and
116 thus in the experiments in VGAT-Venus rats with visible GC spines an accidental activation
117 of PV neurons is yet less likely to occur.
118 TPU of glutamate resulted in consecutive triggered responses and failures in MCs (Fig. 1B).
119 Responses were classified as triggered if they were observed repeatedly within the same
120 time window and showed similar kinetics (see Methods). Next we tested whether these
121 triggered responses were indeed GABAergic by applying the $GABA_AR$ antagonist Bicuculline
122 (BCC, 50 µM), which invariably blocked responses completely (Fig. 1C, n = 7, P < 0.01,
123 Wilcoxon test). Thus in the following the triggered events are denoted as urIPSCs (**u**ncaging-
124 evoked **r**eciprocal IPSCs). Sufficient stability of such urIPSC responses was established via
125 long-term recordings (see Methods). The mean amplitudes of responses during the first and
126 last 5 -10 photostimulations (with at least 10 min in between to mimic the time course of
127 pharmacological manipulations) were not significantly different (Fig. 1E, n = 7, ratio last to
128 first 0.95 ± 0.15, P = 0.74).
129 The amplitude of triggered urIPSCs was on average 12 ± 8 pA, with a rise time of 6 ± 3 ms
130 (in n = 32 MCs clamped to +10 mV), which is significantly smaller than the mean amplitudes
131 of spontaneous IPSCs (n = 14; 22 ± 12 pA; P < 0.001, Mann-Whitney test, Fig. 1F). Since

132 spontaneous IPSCs are highly likely to also originate from the reciprocal MC-GC circuit (see
133 Discussion), this observation argues against overstimulation with glutamate in our
134 experiment. The average release probability from the reciprocal spine was estimated as P_r =
135 0.34 ± 0.11 (Fig. 1F, range 0.13 - 0.60, based on n = 44 MCs, see Methods and Discussion).
136 The latencies of urIPSPCs were not normally distributed, with a first peak within the first 10
137 ms post TPU onset (n = 13), a second peak around 30 ms (n = 19 within the range 10-50
138 ms) and a yet more delayed tail (n = 3; Fig. 1F).
139 In most experiments we detected asynchronous urIPSCs following the first triggered event
140 which were quantified via integral analysis and counting of events (Fig. 1D, see Methods).
141 Both area and number of events increased highly significantly in the 500 ms interval following
142 TPU ('post') compared to the same interval right before ('pre'; mean increase of integrated
143 activity Δ_area + 0.50 ± 0.55 relative to 'pre' value; mean increase in event number + 0.25 ±
144 0.37 relative to 'pre' value; n = 27, P < 0.001 for both; absolute values in 'pre' area 2.40 ±
145 1.83 pAs, events 26.1 ± 14.9). Δ_area was also significantly increased if the extra area of the
146 synchronous urIPSC was subtracted (P < 0.005). Thus asynchronous recurrent inhibition can
147 be already triggered by single glutamatergic inputs.
148 From all these experiments we conclude that local, unitary-like TPU of glutamate can indeed
149 trigger the fast reciprocal release of GABA, providing proof that the reciprocal microcircuit
150 can be activated by single synaptic inputs at physiological levels of Mg^{2+}.
151 *Sodium channel activation is required for most urIPSCs*
152 Next, we investigated a possible contribution of Na_v activation to urIPSC generation. Fig. 2
153 illustrates that wash-in of TTX (500 nM) substantially reduced both triggered and
154 spontaneous events. On average, urIPSC amplitudes were reduced to a fraction of 0.17 ±
155 0.34 of control (Fig. 2D, n = 12, P < 0.005; absolute control amplitudes for -70 mV: -7.8 ± 3.6
156 pA, for 10 mV: 15.4 ± 12.4 pA), and the increase in integrated activity Δ_area was decreased
157 to 0.28 ± 0.21 of its control value (see Methods; n = 10, P < 0.005).
158 Spontaneous sIPSC frequency was also strongly decreased in TTX, to a fraction of 0.24 ±
159 0.17 of control (Fig. 2E, n = 10, P < 0.005).
160 Thus Na_vs are essential to trigger GABA release from the reciprocal spines.
161 *High-voltage activated Ca^{2+} channels in the spine trigger GABA release*

162 HVACCs have been implied to mediate recurrent release from reciprocal spines (Isaacson,
163 2001) and are activated by Na_vs, contributing a substantial fraction to the total postsynaptic
164 Ca^{2+} signal in the GC spine (Bywalez et al., 2015). To directly test whether HVACC activation
165 is required for release of GABA, we blocked NPQ type Ca^{2+} channels with 1 μM ω-conotoxin
166 MVIIC (CTX; Bloodgood and Sabatini, 2007; Bywalez et al., 2015).
167 Fig. 3 shows the resulting substantial decrease of urIPSCs to a fraction of 0.08 ± 0.14 of
168 control (from a mean amplitude of 11.3 ± 5.7 pA; n = 8, P < 0.005, Fig. 3D). This decrease
169 was not different from the effect of TTX on urIPSC amplitude described above (P = 0.35
170 ratios in CTX vs TTX). Δ_area decreased to 0.39 ± 0.23 of control (n = 9, P < 0.005, Fig. 3D),
171 again not different from the effect of TTX on Δ_area described above (P = 0.15 vs TTX).
172 Spontaneous sIPSC frequency in CTX was decreased to a fraction of 0.53 ± 0.15 of control,
173 less markedly than in TTX (Fig. 3E, n = 7 cells, control vs CTX: P < 0.01; CTX vs TTX: P <
174 0.005).
175 We conclude that HVACC activation is required for both fast and slow release of GABA from
176 the reciprocal spine following local input.
177 *NMDA receptors are also relevant for recurrent release*
178 NMDARs are known to substantially contribute to unitary synaptic transmission and to
179 postsynaptic Ca^{2+} entry at the MC to GC synapse (Isaacson and Strowbridge, 1998;
180 Schoppa et al., 1998; Isaacson 2001; Egger et al., 2005). However, because NMDAR-
181 mediated Ca^{2+} entry into GC spines did not depend on Na_v activation in our previous study
182 (in contrast to HVACC-mediated Ca^{2+} entry, Bywalez et al., 2015), and because of the strong
183 blocking effects of TTX or CTX on urIPSCs reported above, we hypothesized that NMDAR
184 blockade would have only mild effects on fast recurrent release upon single inputs.
185 Intriguingly however, Fig. 4 shows that the application of 25 μM D-APV resulted in a
186 substantial decrease of urIPSC amplitudes, to on average 0.22 ± 0.21 of control (from a
187 mean amplitude of 13.8 ± 8.6 pA, n = 10, P < 0.002, Fig. 4D). All individual experiments
188 showed the amplitude decrease, albeit to a variable degree (range 0.00 - 0.68 of control).
189 Δ_area following TPU decreased to 0.40 ± 0.28 of control (n = 10, P < 0.003, Fig. 4D). Both
190 effects were statistically not different from the effects of either TTX or CTX (amplitude: P =
191 0.12 and P = 0.08; Δ_area: P = 0.19 and P = 0.47).

192 APV also substantially reduced spontaneous activity, to a frequency of 0.19 ± 0.08 of control
193 (n = 9, P < 0.01, Fig. 4E), similar to that in TTX (P = 0.84) and significantly more pronounced
194 than that in CTX (P < 0.001).
195 Since the strength of the effect of NMDAR blockade on urIPSCs was surprising to us, we
196 sought to provide another line of evidence for these findings in an experimental setting that
197 does not involve uncaging of glutamate (which might preferentially activate NMDARs, see
198 Discussion). The afterhyperpolarization (AHP) following single MC APs elicited by somatic
199 current injection was found to mainly reflect recurrent inhibition in brain slices from adult
200 mouse (Nunes and Kuner, 2018), while in juvenile rat inhibitory synaptic contributions to the
201 AHP were observed to be less substantial but still detectable (on the order of 20-30% relative
202 to the K^+ channel-mediated component, Dumenieu et al., 2015). We used this paradigm to
203 test whether NMDAR blockade alone could interfere with recurrent inhibition (Fig. 4F). Single
204 MC AP AHPs (n = 13 MCs, V_{hold} = -70 mV) had a mean amplitude ΔV_m = – 9.5 ± 2.1 mV and
205 a mean half duration $t_{1/2}$ = 43 ± 25 ms. Fig. 4G shows that APV application significantly
206 reduced the mean AHP amplitude to a fraction of 0.86 ± 0.12 of control (P < 0.001, Wilcoxon
207 test; reduction in 12 of 13 MCs), while the half duration was not changed (fraction of control
208 1.02 ± 0.42, P = 0.65). Next, to block $GABA_A$Rs we turned to gabazine (GBZ, 20 µM), since
209 BCC might affect the K^+ channels that contribute to slow AHPs (Khawaled et al. 1999,
210 Dumenieu et al. 2015). GBZ alone caused a slightly stronger reduction than APV which was
211 not significantly different (to 0.71 ± 0.10 of control, n = 7 MCs, P = 0.08 vs APV, not shown).
212 Occlusion experiments using APV before GBZ or GBZ before APV did result in no further
213 reduction (0.98 ± 0.10 of amplitude in presence of first drug, n = 8 MCs, P = 0.45, Fig. 4F,G).
214 Thus these experiments further support a substantial role of GC NMDARs for GABA release.
215 From these and the uncaging experiments we conclude that NMDARs located on GCs are
216 strongly involved in reciprocal release, even though prevention of HVACC activation (via Na_v
217 block or pharmacology) also blocks reciprocal release. What is the underlying mechanism?
218 The simplest explanation for a fast cooperation would be a summation of NMDAR- and
219 HVACC-mediated Ca^{2+} currents at the presynaptic Ca^{2+} sensor. For this scenario two
220 requirements need to be satisfied: (1) temporal overlap of Ca^{2+} currents and (2) spatial
221 proximity of NMDARs and HVACCs within the same microdomain.

222 *Temporal overlap: Simulations of GC spine Ca^{2+} currents via HVACCs and NMDARs*

223 In conventional glutamatergic synapses the NMDAR-mediated postsynaptic current is rising
224 rather slowly compared to the AMPAR-mediated component (rise time ~ 10 ms, Lester et al.
225 1990) and therefore the fractional NMDAR Ca^{2+} current seems at first an unlikely candidate
226 to make direct contributions to fast release. In the reciprocal GC spines however, Na_v
227 channels are locally activated, which enables fast and substantial NMDAR activation. Fig. 5A
228 shows a simulation of the postsynaptic NMDAR- and HVACC-mediated Ca^{2+} currents (based
229 on the detailed NEURON model described in Aghvami et al. 2019, see Methods) which
230 illustrates that the local AP causes a transient boosting of the NMDAR Ca^{2+} current because
231 of further relief of the Mg^{2+} block during the upstroke and overshoot of the spine spike.
232 According to the simulation this fast NMDAR-mediated Ca^{2+} spikelet begins even before the
233 HVACC-mediated current and tightly overlaps with it within > 1 ms. Thus HVACC- and
234 NMDAR-mediated Ca^{2+} currents could act in a cooperative manner at the Ca^{2+} sensor(s) that
235 mediate fast release of GABA, especially so, if the release probability was proportional to the
236 fourth power of local $\Delta[Ca^{2+}]$ or more as at other central synapses, and if the channels were
237 close enough to form a microdomain, allowing for an 'overlap bonus' (Stanley 2016, Fig. 5B).
238 In the temporal domain, this overlap was found to be highly robust against the variation of the
239 combined Na_v/K_v conductance, and increases in either AMPAR conductance g_{AMPA} or neck
240 resistance R_{neck} resulted in an earlier activation of both HVACC and NMDAR-mediated Ca^{2+}
241 currents and even stronger overlap (Fig. 5C, see Methods). Decreases resulted at first in
242 little change and then a loss of the spine spike whereupon there is no more HVACC
243 activation. To illustrate specifically the contribution of the Na_v-mediated boosting of the
244 NMDAR-mediated Ca^{2+} current, we also calculated the overlap bonus for the HVACC-
245 mediated current as above and the NMDAR current in absence of the spine spike, which
246 indeed renders the cooperative effect negligible (Fig. 5B).

247 *Spatial proximity: Ultrastructural evidence for presynaptic localization of NMDARs*

248 For fast neurotransmitter release to occur, the current view is that Ca^{2+} entry needs to
249 happen in a proximity of 100 nm or less from the Ca^{2+} sensing part of the SNARE machinery
250 (reviewed in Kaeser and Regehr, 2014; Stanley 2016). Therefore, to permit cooperation of
251 Ca^{2+} influxes, NMDARs should be localized very close to or within the GABAergic

252 presynapse. Earlier electron microscopic (EM) studies had reported the presence of
253 postsynaptic NMDARs in GC spines and observed also extrasynaptic labeling (Sassoè-
254 Pognetto & Ottersen 2000, Sassoè et al. 2003). To test for the presence of NMDARs near or
255 within GABAergic active zones, we analysed GC spine heads in ultrathin sections that were
256 immunogold-labeled with either GluN1 or GluN2A/B antibodies (Fig. 6A; see Methods); the
257 sections were selected for the presence of at least one asymmetric (i.e. glutamatergic)
258 contact and/or one symmetric (i.e. GABAergic) contact.
259 Interestingly, we observed that when both symmetric and asymmetric synaptic profiles were
260 visible in individual GC-MC dendrodendritic pairs, the two synaptic profiles were mostly either
261 contiguous (44% of n = 60 cases, examples Fig. 6A2,A3, cumulative plot Fig. 6B) or closer
262 than 100 nm (36% of cases). This observation implies that on both sides of the
263 dendrodendritic synaptic arrangement the postsynaptic specialization very often merges with
264 presynaptic release sites without interposition of non-synaptic membrane domains, and that
265 on the GC side postsynaptic NMDARs can be located very closely to the GABAergic
266 presynapse.
267 Immunogold labeling for NMDARs was also frequently observed in symmetric contacts, albeit
268 at a lesser density compared to asymmetric contacts (Fig. 6A). To establish whether there is
269 an increased likelihood for the presence of NMDARs at symmetric contacts, we compared
270 the densities of labeling in non-synaptic membrane segments of GC spines with those in
271 symmetric synapses, and as a control in asymmetric synapses. GC spines establishing
272 synapses with MC dendrites were selected as described (see Methods) and all discernible
273 membrane segments within a spine were analysed. For GluN1, there were 50 particles along
274 84.5 µm of 138 non-synaptic spine membrane segments (mean 0.6 particles/µm), 70
275 particles along 32.7 µm of 120 symmetric profiles (mean 2.1 particles/µm) and 394 particles
276 along 28.6 µm of 111 asymmetric profiles (mean 13.8 particles/µm). Fig. 6C shows the
277 density distributions across the three types of membrane segments. The distribution of the
278 density of gold particles at symmetric synapses was significantly higher than the one in non-
279 synaptic membrane (P = 0.000029, Kolmogorov-Smirnov test). For GluN2A/B, the sample
280 size was smaller, with 5 particles along 10.0 µm of 24 non-synaptic spine membrane
281 segments (mean 0.5 particles/µm), 89 particles along 14.0 µm of 46 symmetric profiles

282 (mean 6.4 particles/µm) and 96 particles along 6.1 µm of 25 asymmetric profiles (mean 15.7
283 particles/µm). Still, the density distribution at symmetric synapses was significantly higher
284 than the distribution at the non-synaptic membrane (P = 0.000048). Interestingly, the labeling
285 densities for GluN1 and also GluN2A/B were similar across non-synaptic membranes and
286 asymmetric synapses (P = 0.99 and P = 0.81, respectively). However, labeling of symmetric
287 synapses was considerably stronger for GluN2A/B versus GluN1 (P = 0.00042). This
288 difference might be due to a distinct receptor configuration and/or a better accessibility of the
289 GluN2 epitopes in the presynaptic symmetric membrane.
290 Finally, we analysed the radial distribution of particles across synaptic profiles for both
291 antibodies to establish whether labeling was predominantly associated with either the GC or
292 the MC membrane (Fig. 6D; see Methods). The distribution of both GluN1 and GluN2A/B
293 label at asymmetric synapses was similar, with a main peak just inside the postsynaptic GC
294 membrane and another peak within the synaptic cleft. Only a few gold particles were
295 localized beyond 20 nm on the MC side, suggesting that NMDARs are not expressed at
296 significant levels at the glutamate release sites on the MC membrane. Notably, the
297 distribution of gold particles at symmetric synapses mirrored the one at asymmetric
298 synapses, implying that labeling for NMDARs is predominantly associated with both the
299 presynaptic GABAergic and the postsynaptic glutamatergic membrane of GCs.
300 In summary, we conclude from these findings that NMDARs do play a direct presynaptic role
301 for recurrent release of GABA.
302

303 ***Discussion***

304 Here we have demonstrated that mimicking unitary synaptic inputs via two-photon uncaging
305 of glutamate onto individual olfactory bulb GC spines can activate the entire microcircuit
306 within the spine, from the local spine spike to the release of GABA onto MC lateral dendrites,
307 proving the mini-neuron-like functionality of the reciprocal microcircuit. As in classical axonal
308 release, sequential Na_v channel and HVACC activation triggers output, which occurs on both
309 fast and slow time scales. Strikingly, however, NMDA receptors are also found to play a
310 presynaptic role for GABA release.

311 *Properties of microcircuit operation*

312 For the proximal reciprocal GC inputs investigated here we estimate that under physiological
313 conditions close to the MC resting potential the size of the fast IPSCs is on the order of -5
314 pA, after corrections for the partial $GABA_AR$ block by DNI and the setting of E_{Cl}. Thus,
315 assuming an *in vivo* MC input resistance of 100 MΩ (Angelo and Margrie, 2011), a single
316 GC-mediated IPSC will exert a somatic hyperpolarization of at best 0.5 mV. Thus proximal
317 single GC spine inputs are likely to play a rather subtle role in influencing MC firing
318 (Fukunaga et al., 2014; McIntyre and Cleland, 2016) - unless there is coordinated activity
319 across GC spines connected to the same MC dendrite, for example in the wake of an MC
320 action potential during the recurrent IPSP (see e.g. Fig. 4F), during gamma oscillations (e.g.
321 Kay, 2003; Lagier et al., 2004) or due to 'super-inhibitory connectivity' as predicted by Gilra
322 and Bhalla (2015).

323 Upon local activation we observed a release probability P_r from the GC spine on the order of
324 0.33. This P_r value might represent an upper limit, because the global reduction of inhibition
325 by DNI could cause a homeostatic upregulation of P_r at GABAergic synapses (e.g. Rannals
326 and Kapur, 2011). Moreover there is a general bias for detection of connections with larger P_r
327 due to high levels of spontaneous activity and the limited recording time. However, since our
328 experiments were conducted at room temperature, physiological temperatures might
329 counterbalance such effects.

330 With $P_{r_GABA} \approx 0.3$ and the probability for MC glutamate release on the order of $P_{r_Glu} \approx 0.5$ –
331 0.75 (Egger et al., 2005; Pressler and Strowbridge, 2017) the efficiency of the entire
332 reciprocal microcircuit can be estimated as $P_{reciprocal} = P_{r_Glu} \cdot P_{r_GABA} \approx 0.2$, possibly informing

333 future network models of bulbar interactions. The rather low P_{r_GABA} observed here also
334 implies that GC spines might be enabled to release with higher probabilities by coincident
335 global GC signalling (Ca^{2+} spike or global AP), due to increased ΔCa^{2+} in the spine (Egger et
336 al., 2005; Egger, 2008; Aghvami et al., 2019).
337 As to the minimal latency for GABA release, the temporal resolution of our experiments is
338 limited by the duration of the uncaging pulse (1 ms) and by not knowing the membrane
339 potential time course $V_m(t)$ in the GC spine. Fig. 1E shows that the fastest urIPSCs were
340 detected within 2 ms from TPU onset, implying that there is a fast mechanism coupling Ca^{2+}
341 entry to release. Earlier, tight coupling between Ca^{2+} entry and GABA release has been
342 demonstrated at this synapse using EGTA (Isaacson, 2001), and a crucial role for Na_v
343 channels has been suggested (Bywalez et al., 2015; Nunes and Kuner, 2018), both
344 confirmed by our present results.
345 While ~ 30% of urIPSCs occurred within 10 ms post TPU onset, there was also a substantial
346 fraction with longer latencies in the range of 10 - 30 ms and some even larger delays.
347 Substantial asynchronous release from the GC spine on yet longer time scales (detected at
348 up to 500 ms post TPU) was frequently observed. Thus with regard to temporal processing
349 the microcircuit is capable of operating across a wide range of latencies, which might
350 contribute to glomerulus-specific GC global AP firing latencies (Kapoor and Urban, 2006),
351 and also of generating combined synchronous and asynchronous output.
352 *Na_v-mediated and NMDAR-mediated contributions to release*
353 How is postsynaptic Ca^{2+} entry coupled to release of GABA within the GC spine? Previously
354 we have shown via occlusion experiments that Ca^{2+} entry via NMDARs occurs independently
355 from Ca^{2+} entry mediated by the Na_v-HVACC pathway, since AMPAR-mediated
356 depolarization on its own is strong enough to lift the Mg^{2+} block, probably due to boosting by
357 the high GC spine neck resistance (Bywalez et al., 2015). Therefore we hypothesized that
358 the Na_v-HVACC pathway would provide the sole trigger for fast release of GABA, as in
359 classical release from axons (see also the recent findings on GC Na_v 1.2 by Nunes and
360 Kuner, 2018), reinforcing the notion of the GC spine as an independent mini-neuron that can
361 generate output via its own local AP. Indeed, blockade of either Na_v or HVACCs strongly
362 reduced or abolished urIPSCs. However, in subsequent experiments probing NMDAR

363 contribution we observed that urIPSCs were massively reduced by blockade of NMDARs as
364 well.
365 As a note of caution, activation of single GC spines via TPU might involve spurious activation
366 of extrasynaptic NMDARs, since at the large GC spines the TPU volume does not
367 necessarily precisely match the location of the glutamatergic postsynapse. We also observed
368 that TPU resulted in a slightly larger NMDA-receptor mediated component of the
369 postsynaptic Ca^{2+} signal than true synaptic activation via glomerular stimulation (~ 65 % vs ~
370 50% of ΔF/F, Bywalez et al., 2015; Egger et al., 2005). Thus at least part of the strong impact
371 of NMDARs observed here might have been rooted in their over-activation. Therefore we
372 investigated recurrent inhibition elicited by single MC APs, and could demonstrate that
373 NMDAR blockade alone (which does not prevent GC spine spike generation, see Bywalez et
374 al., 2015) also reduces recurrent inhibition. This effect was found to be mutually occlusive
375 with the effect of $GABA_AR$ blockade, arguing again in favor of an essential role of NMDARs
376 for GABA release.
377 In our previous study of postsynaptic Ca^{2+} signals in GC spines there was no obvious
378 influence of Na_v activation on NMDAR-mediated Ca^{2+} entry (Bywalez et al. 2015). At first, this
379 finding might seem at variance with the current simulations in Fig.5 that demonstrate a
380 boosting of early NMDAR-mediated Ca^{2+} currents by the spine spike. However, the
381 simluations also indicate that this extra contribution is not substantial in terms of added ΔF/F
382 under our experimental conditions and therefore could not be detected (Fig. 5D).
383 In line with the fast NMDAR-mediated Ca^{2+} spikelet, Kampa et al. (2004) have shown that the
384 earlier the postsynaptic membrane is depolarized after glutamate release, the more
385 efficiently NMDARs will be activated. These observations are of general importance in the
386 context of spike-timing dependent plasticity and electrical compartmentalization of spines
387 (e.g. Grunditz and Oertner, 2004, Tonnesen and Nägerl, 2016).
388 How exactly do NMDARs now effect release? The Na_v/NMDAR-mediated Ca^{2+} spikelet
389 results in substantial and fast coincident activation of NMDARs and HVACCs, and our
390 ultrastructural evidence for presynaptic NMDARs implies that indeed these currents can feed
391 into the same presynaptic microdomain (see Results). This overlap bonus at the presynaptic

392 Ca^{2+} sensor (as predicted by the simulations) is likely to underlie the observed cooperative
393 signalling of HVACCs and NMDARs.

394 *Direct involvement of presynaptic NMDARs in GABA release*

395 Presynaptic actions of NMDARs at specific subsets of both glutamatergic and GABAergic
396 synapses have recently received attention (reviewed in Bouvier et al., 2015; Banerjee and
397 Paulsen, 2016). Presynaptic NMDARs have been shown to play a role in plasticity induction
398 (e.g. Duguid and Smart, 2004) or in modulation of basal synaptic transmission, where effects
399 are mostly observed upon repetitive transmitter release (e.g. McGuiness et al. 2010).
400 Presynaptic NMDARs in the cerebellum are also involved in enhancing spontaneous release
401 of GABA (Glitsch and Marty, 1999), and similar observations have recently been made for
402 extrasynaptic NMDA receptors on retinal A17 amacrine cells (Veruki et al., 2019). However,
403 to our knowledge direct triggering of release during unitary transmission via presynaptic
404 NMDARs has not been observed so far, adding another pathway to the already highly
405 diverse signalling downstream of NMDARs.

406 The observed cooperation between Na_v/HVACCs and NMDARs relates our study back to the
407 initial studies on dendrodendritic recurrent inhibition (DDI), when it was concluded by several
408 groups that NMDARs can contribute directly to release from the reciprocal spine upon
409 extended release of glutamate from the MC dendrite (see Introduction), and Schoppa et al.
410 (1998) already speculated that this presynaptic function might be related to either Ca^{2+} entry
411 or depolarization, favoring the latter possibility. However, the relative contribution of
412 NMDARs has been under debate and it was demonstrated that under physiological
413 conditions HVACC activation would be the dominant release trigger (Isaacson 2001). While
414 the standard DDI protocol, using 20-50 ms long depolarizations, would evoke recurrent
415 inhibition also in the presence of TTX (possibly even enhanced, Halabisky et al., 2000), it
416 was reported by two groups that recurrent inhibition in response to shorter steps (< 5 ms) is
417 substantially smaller than for the long step and reduced in TTX (Schoppa et al., 1998;
418 Halabisky et al., 2000). In view of our finding of the spine spike and its ability to trigger
419 release these observations can be explained such that the standard DDI protocol can recruit
420 NMDAR-dependent pathways for triggering GABA release via prolonged release of
421 glutamate and the subsequent summation of EPSPs in GC spines, whereas short stimulation

422 is more likely to trigger release via the GC spine spike. Thus the cooperation of NMDARs
423 and HVACCs reconciles the conflicting earlier findings.
424 Ultimately, what is the advantage of this cooperative release mechanism for recurrent
425 processing? At this point, we can merely guess that perhaps the involvement of presynaptic
426 NMDARs allows the mini-neuron to incorporate extra modulatory mechanisms that it is
427 otherwise deprived of, since its compact arrangement prevents any modulatory interference
428 known to occur in conventional neurons during the classical steps of integration from the
429 synapse via the dendrite to the axon hillock.
430 *Reciprocal inhibition and spontaneous inhibitory activity*
431 Since MCs with truncated tufts do not show a reduced sIPSC frequency (Arnson and
432 Strowbridge, 2017), sIPSCs are likely to predominantly originate from the more proximal
433 lateral MC dendrites and consist of GC inputs. The larger mean amplitude of sIPSCs
434 compared to triggered urIPSCs observed here might be explained by perisomatic inhibitory
435 contacts onto MCs, e.g. by type S GCs (Naritsuka et al. 2009) or connections from other
436 bulbar inhibitory interneuron types that might feature stronger synapses and/or several
437 contacts. All three antagonists of urIPSC generation (TTX, CTX, APV) were found to also
438 substantially reduce spontaneous IPSC frequency. In the case of Na_v blockade, strong
439 effects on MC sIPSCs were also reported elsewhere (e.g. Halabisky et al., 2000; Arnson and
440 Strowbridge, 2017) and are expected because of the blockade of spontaneous MC firing and
441 thus a decrease in the excitation levels also of synaptically connected inhibitory neurons; in
442 particular, the blockade of the GC spine spike will prevent recurrent GABA release upon
443 spontaneous release of glutamate from MC lateral dendrites onto GC spines. The effect of
444 HVACC blockade was less pronounced than that of Na_vs, probably because it will not
445 prevent spontaneous MC firing and thus have less of an effect on global network activity.
446 The substantial effect of NMDAR blockade on spontaneous IPSCs was also observed in
447 other olfactory bulb studies (Wellis and Kauer, 1993; Schmidt and Strowbridge, 2014). Part
448 of the strong contribution of NMDARs may be related to the long-lasting depolarizations
449 observed in MCs that are enhanced in amplitude and duration by NMDARs (Carlson et al.,
450 2000) and in our hands often increased their frequency in the presence of DNI. MC NMDA
451 autoreceptors might also contribute (see Introduction). Finally, the crucial role of NMDARs for

452 release from the GC spine reported here explains why spontaneous release of glutamate
453 from MCs is unlikely to trigger recurrent IPSCs in the presence of APV. Thus the strong
454 effect of APV on sIPSCs is also in line with the presynaptic function of NMDARs.

455 *Functional role of local reciprocal processing*

456 While there is first evidence for substantial dendritic Ca^{2+} signals and local GC spine signals
457 *in vivo* (Wienisch and Murthy, 2016; Wallace et al., 2017; Zhang et al., 2016), the extent to
458 which specifically local GABA release from GC spines contributes to odor processing in the
459 olfactory bulb is difficult to estimate at this point. Although global GC spiking is probably not
460 required for the generation of gamma oscillations (Lagier et al., 2004), the precise role of
461 gamma in odor processing is not yet clear. It is tempting to speculate that local recurrent
462 feedback might allow for glomerular columns to act as independent oscillators.

463 Both GC NMDARs and Na_vs are known to play a role specifically in discriminations between
464 binary odorant mixtures, since in the same behavioral paradigm GC-specific knock-down (in
465 about ~ 50% of GCs) of GluN1 resulted in an increase in discrimination time of on average ~
466 60 ms, and knock-down of Na_vs of ~ 85 ms versus control, while discriminations between
467 pure odors were not affected (Abraham et al., 2010; Nunes and Kuner, 2018). However, the
468 relative impact of recurrent inhibition versus lateral inhibition is not clear. Future
469 methodological advances willl be required to tackle the contribution of the GC spine spike
470 along with its cooperative release mechanism to bulbar processing, including voltage-
471 sensitive dye imaging and novel genetic loss-of-function approaches for dissecting local
472 recurrent release from lateral inhibition - perhaps by targeting specifically presynaptic
473 NMDARs. In any case, our data show that fast recurrent inhibition can be triggered by single
474 mitral cell inputs, which may explain the purpose of the granule cell spine spike. We predict
475 that these mechanisms are likely to be of crucial importance for fast bulbar processing.

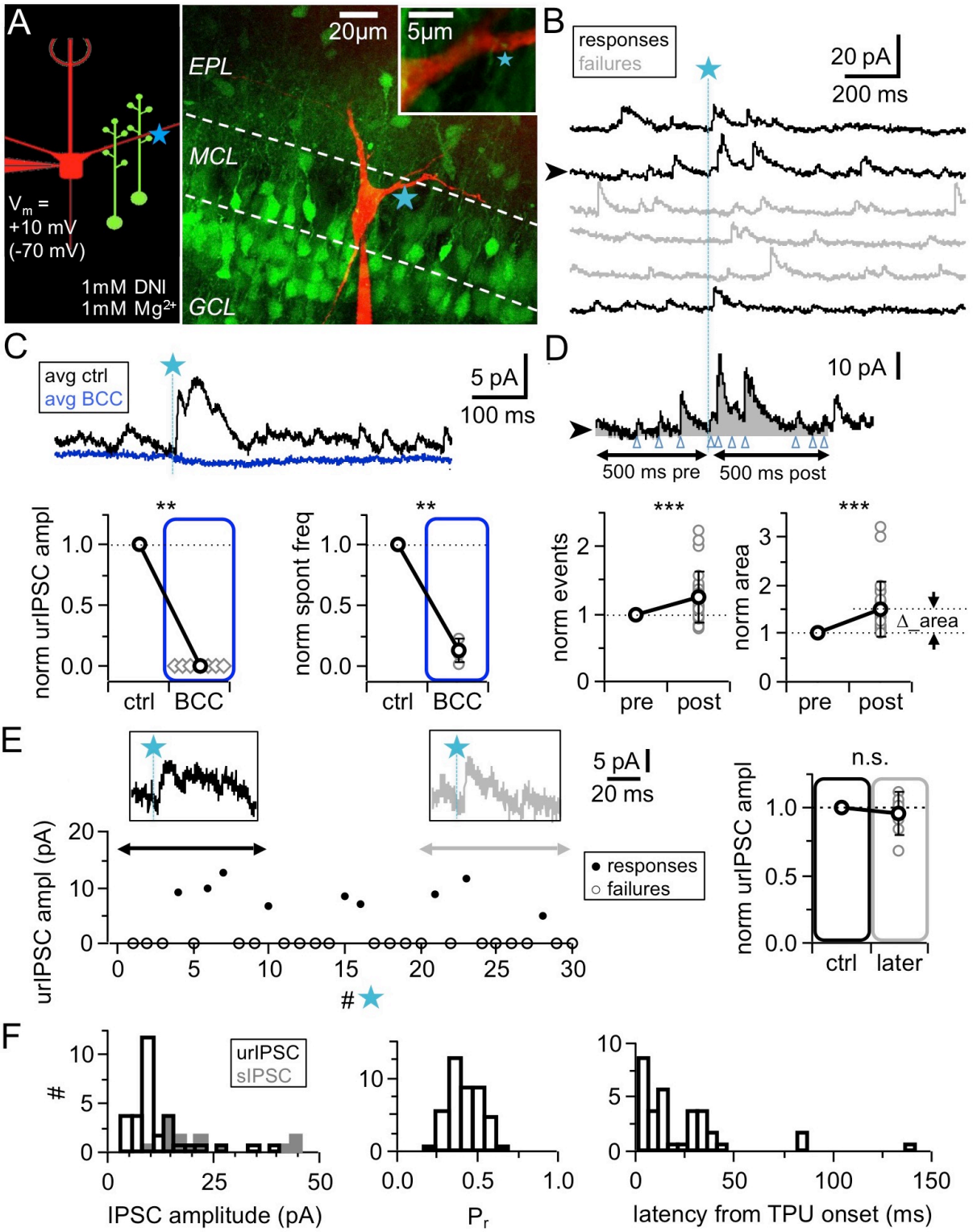

Figure 1. **TPU-induced glutamatergic activation of GC spines triggers GABA release detected as uncaging-evoked reciprocal IPSCs (urIPSCs) in MCs.**

(**A**) Experimental setting (scheme and image): Somatic whole cell voltage clamp recording from MC filled with Alexa 594 (red, 50 µM) and TPU of DNI-caged glutamate (DNI; blue star) at GC spines in VGAT-Venus rats (GCs green).

(**B**) Example of consecutive uncaging traces showing urIPSC responses (black) and failures (grey).

(**C**) Effect of $GABA_AR$ blockade (bicuculline, BCC, 50 µM, blue) on urIPSCs and spontaneous activity. Top: Example experiment, showing averaged traces. Bottom: Cumulative data on urIPSC amplitude (left panel, n =7) and on frequency of spontaneous events (right panel, n = 6).

(D) Analysis of asynchronous events. Top: Example trace from (B) with analysis intervals pre- and post-uncaging (grey areas, black arrows). Counted events marked by blue arrowheads. Bottom: Normalized IPSC event number and area (integrated activity, relative increase vs control Δ) in pre- versus post-uncaging intervals (n = 27, see Methods).

490 (**E**) Stability of urIPSC recordings. Left: Representative experiment showing individual urIPSC
491 amplitude values over consecutive stimulations (1 TPU per min). Insets: Averaged urIPSC responses
492 in the first (black, n = 3 responses) and last ten minutes (grey, n = 3). Right: Comparison of averaged
493 normalized urIPSC amplitudes separated by 10 min interval (n = 7 MCs).
494 (**F**) Properties of first triggered urIPSCs. Left: Amplitudes (n = 32 MCs, V_m = +10 mV). Dark grey:
495 Amplitude distribution of spontaneous IPSCs for comparison (n = 14 MCs, mean amplitudes). Middle:
496 Release probabilities P_r (n = 44). Right: Latencies from TPU onset (n = 36).
497 All Figures: Significance (non-parametric tests): n.s. not significant, * $P < 0.05$, ** $P < 0.01$, *** $P <$
498 0.001; mean data ± S.D.

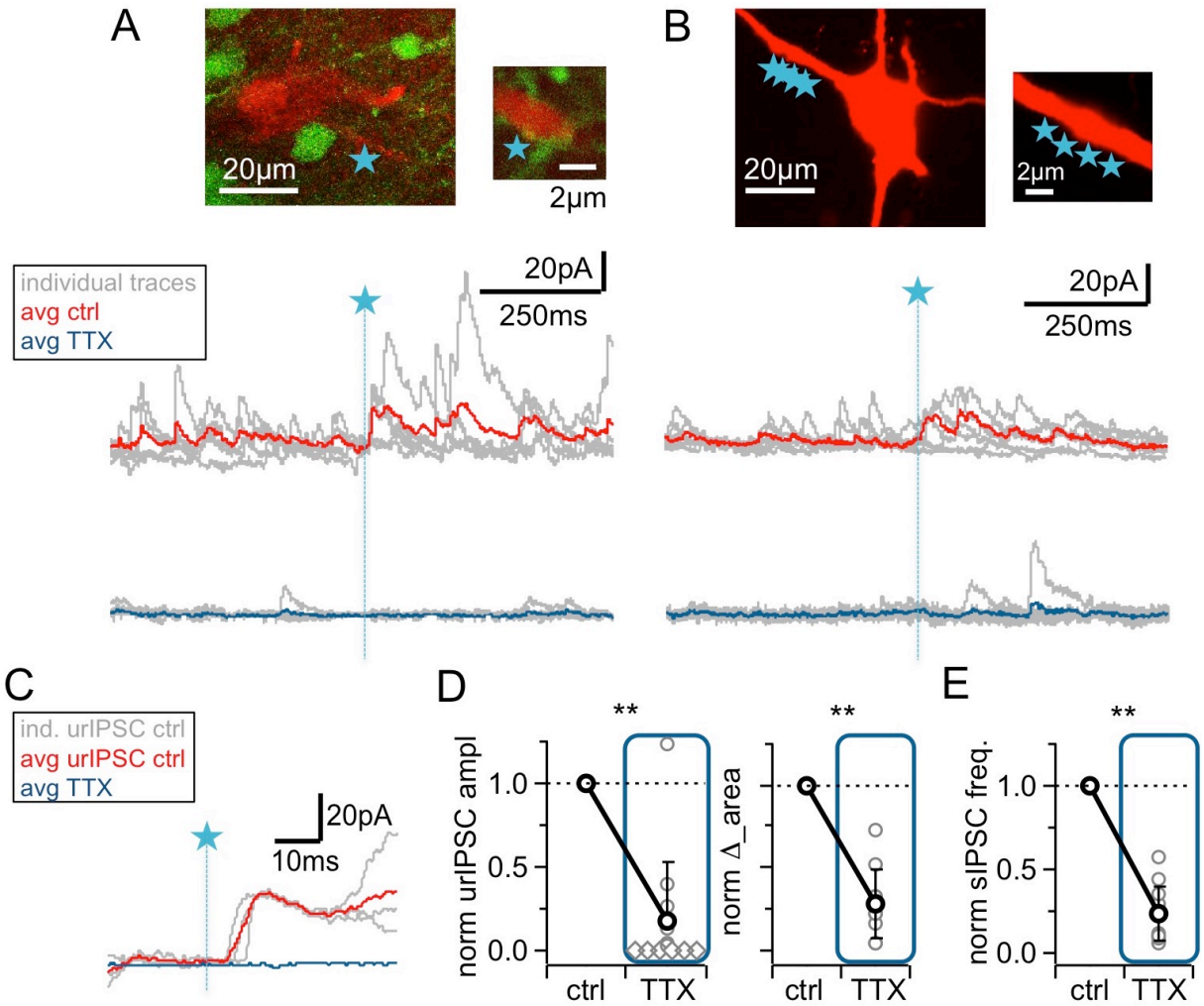

Figure 2. The urIPSC is reduced by Na_v blockade (TTX, 500 nM).
(**A, B**) Representative experiments showing a patch-clamped mitral cell (Alexa594 50 µM, red), the uncaging site(s) along a lateral dendrite (blue star) and below the corresponding uncaging traces with individual traces shown in grey, average control traces in red and average TTX traces indicated in blue (A: VGAT-Venus rat, single-site TPU, B: Wistar rat, multi-site TPU).
(**C**) Magnified illustration of traces in (A) (for control individual traces with urIPSC responses and their average, for TTX only average, color coding as above).
(**D**) Left: Cumulative normalized data showing the strong reduction of urIPSC amplitude during Na_v blockade with TTX (n = 12). Diamonds indicate the experiments with no detectable response in the presence of the drug. Right: Comparison of normalized IPSC Δ_area between control and in the presence of TTX (see Methods, n = 10).
(**E**) sIPSC frequency comparison beween control and in presence of TTX (n = 10). See also A,B.

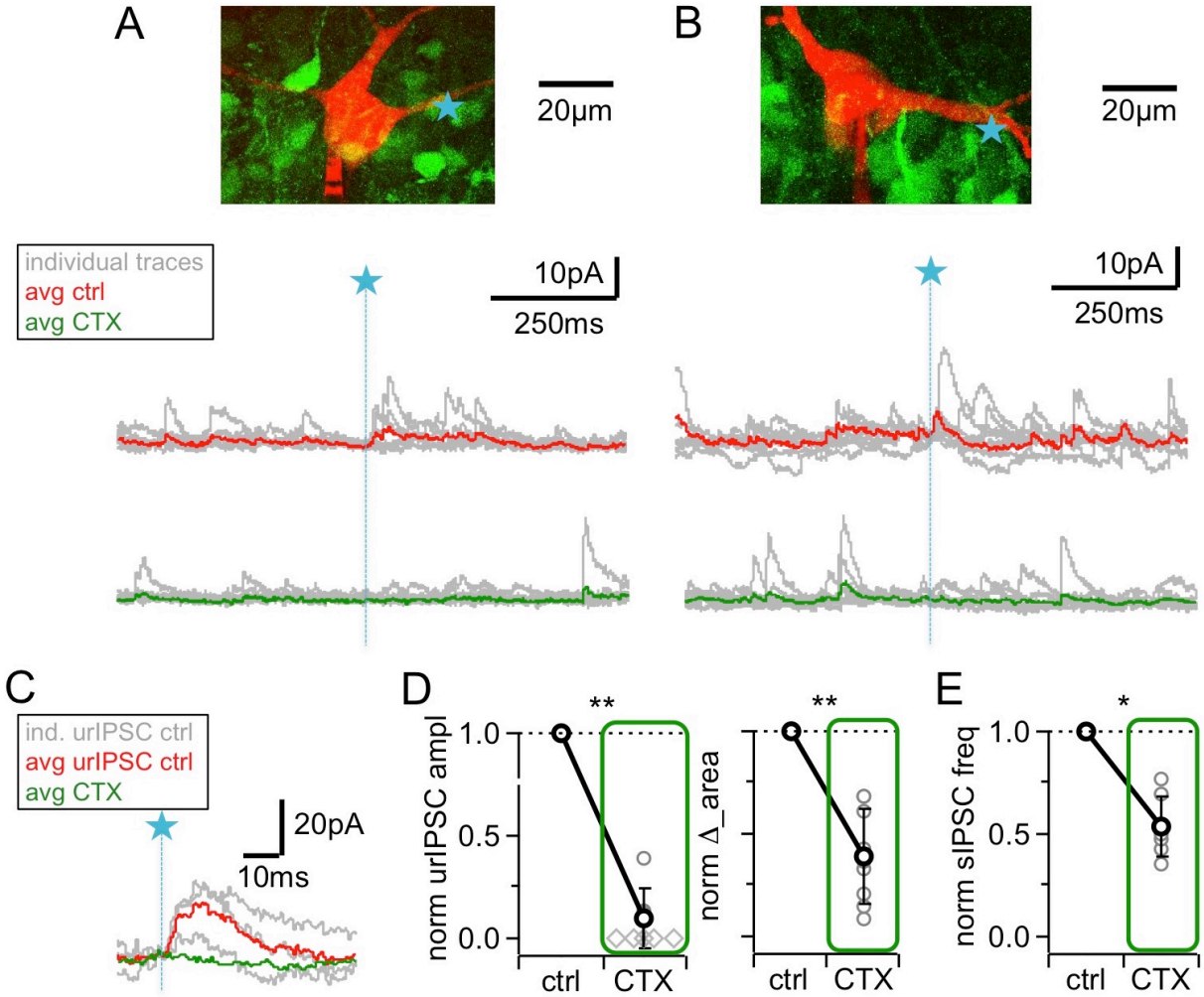

Figure 3. Blockade of high voltage activated Ca^{2+} channels by ω-conotoxin MVIIC (CTX, 1 µM) causes a prominent reduction of urIPSC amplitudes.

(**A, B**) Two representative experiments in brain slices from VGAT-Venus rat with the corresponding MC (red), the site of TPU (blue star) and the uncaging traces according to the condition (individual traces : grey, average control: red, average CTX: green).

(**C**) Left: Magnified illustration of traces in B (for control individual traces with urIPSC responses and their average, for CTX only average, color coding as above).

(**D**) Left: Summary of effects of CTX on average normalized urIPSC amplitude (n = 8). Diamonds indicate the experiments with no detectable response in the presence of the drug. Right: Comparison of delta urIPSC areas normalized to control versus in the presence of CTX (n = 9).

(**E**) Inhibitory effect of CTX on spontaneous IPSC frequency (n = 7). See also A,B.

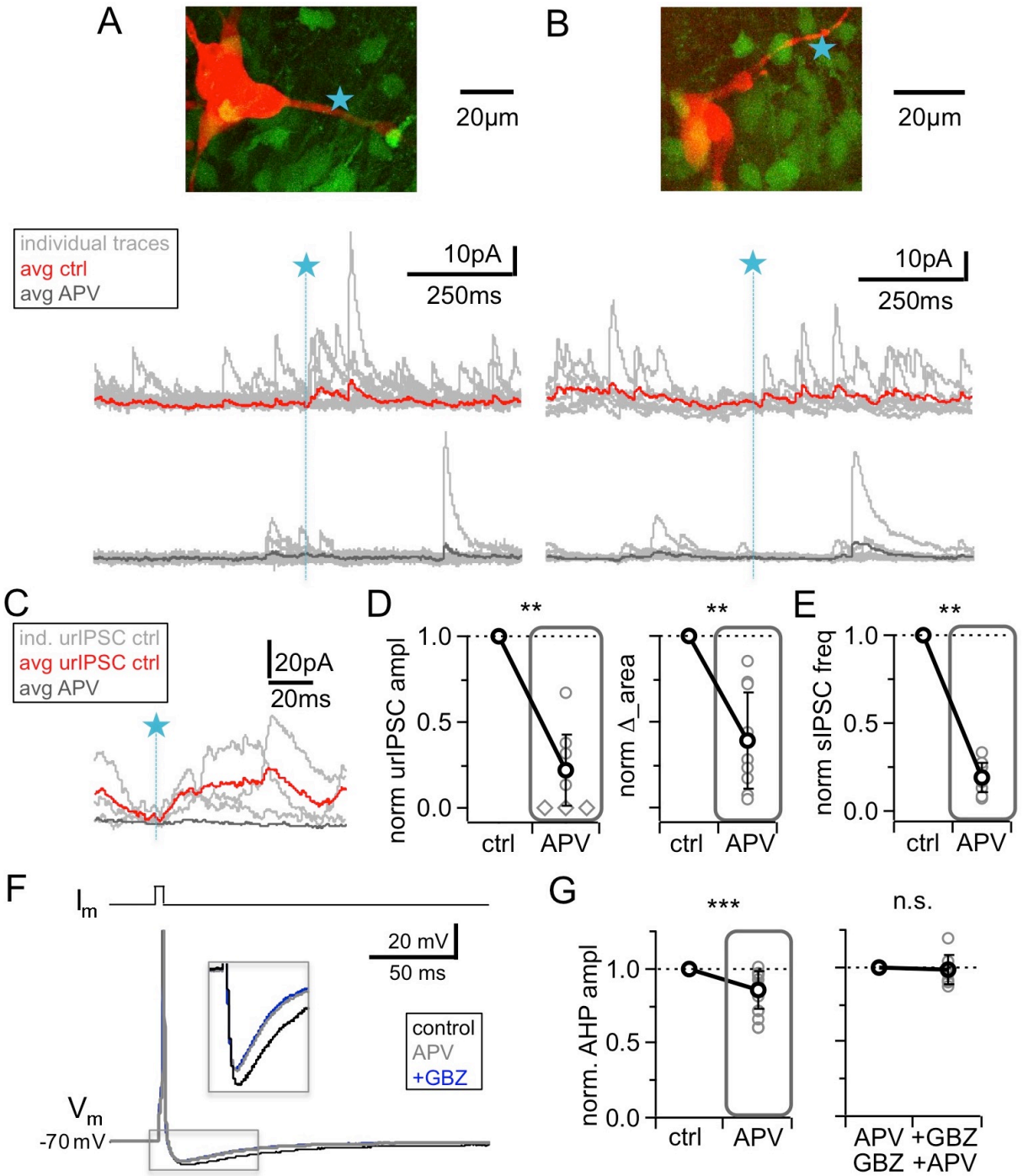

Figure 4. NMDAR blockade with D-APV (25 µM) results in a strong reduction of urIPSC amplitudes and also reduces AHPs following mitral cell APs

(**A, B**) Two representative uncaging experiments with the corresponding MC (red), the site of TPU (blue star) and the uncaging traces according to the condition (individual traces: grey, average control: red, average APV: dark grey); both VGAT-Venus.

(**C**) Magnified illustration of traces in A (for control individual traces with urIPSC responses (grey) and their average (red), for APV only average (dark grey)).

(**D**) Left: Summary of effects of APV on average normalized urIPSC amplitude (n = 10). Diamonds indicate the experiments with no detectable response in the presence of the drug. Right: Comparison of delta urIPSC integrals between control versus in the presence of APV (n = 10).

(**E**) Cumulative effect of APV on spontaneous IPSC frequency; see also A,B (n = 9).

(**F**) Representative example of MC AP evoked by somatic current injection in control conditions (black trace) and in the presence of APV (grey trace) and added GBZ (20 µM; blue trace). Inset: Magnified AHPs.

(**G**) Left: Cumulative effects of APV on average normalized AHP amplitude (n = 11 MCs). Right: Effect of occlusion experiments on AHP amplitude (APV before GBZ or GBZ before APV, n = 8).

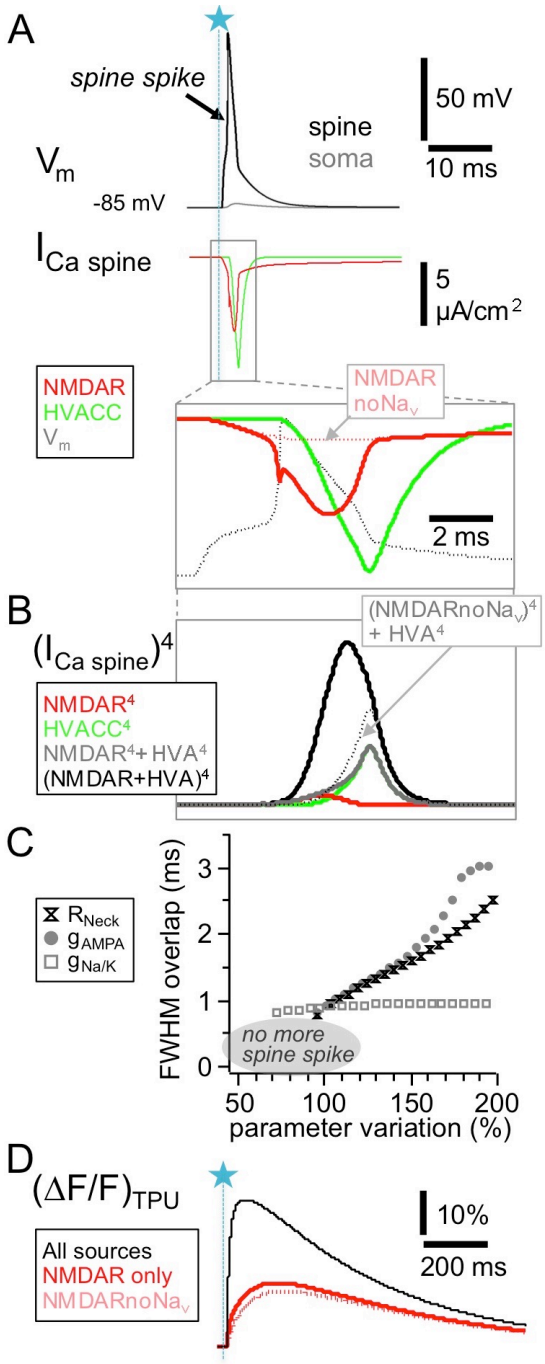

Figure 5. Temporal overlap of HVACC- and NMDAR-mediated Ca^{2+} currents. Simulated spine Ca^{2+} currents and $(\Delta F/F)_{TPU}$

(**A**) Top panels: spine membrane potential V_m and Ca^{2+} currents (as in Aghvami et al. 2019, their Fig 2B, but without exogenous Ca^{2+} buffer). Bottom: Blow-up of NMDAR- and HVACC-mediated Ca^{2+} currents, overlaid with the membrane potential V_m. Note the early onset of the NMDAR Ca^{2+} current and its increase during the underlying local action potential. Red dotted line: NMDAR Ca^{2+} current in the absence of Na_v channels.

(**B**) The temporal coincidence creates an ‚overlap bonus' with respect to local Ca^{2+} concentration and triggering of release: Fourth power of single and added Ca^{2+} currents. Black dotted line: Addition (hypothetical!) of HVACC with NMDAR Ca^{2+} current in the absence of Na_v.

(**C**) Robustness test for extent of overlap between NMDAR- and HVACC-mediated Ca^{2+} current. Overlap is measured as the stretch of overlapping FWHMs of the current transients (Full Width Half Maxima, see Methods). Parameter variation within 50 - 200% of the nominal value of the neck resistance R_{neck}, the AMPAR conductance gAMPA and the coupled Na_v/K_v conductance $g_{Na/K}$. Results are shown only for parameter runs with spine spike.

(**D**) Simulated fluorescence transients ΔF/F (in the presence of 100 µM OGB-1) show that the contribution of the Na_v-mediated boost of NMDAR Ca^{2+} currents to the total NMDAR-mediated Ca^{2+} signal is almost negligible (see Discussion).

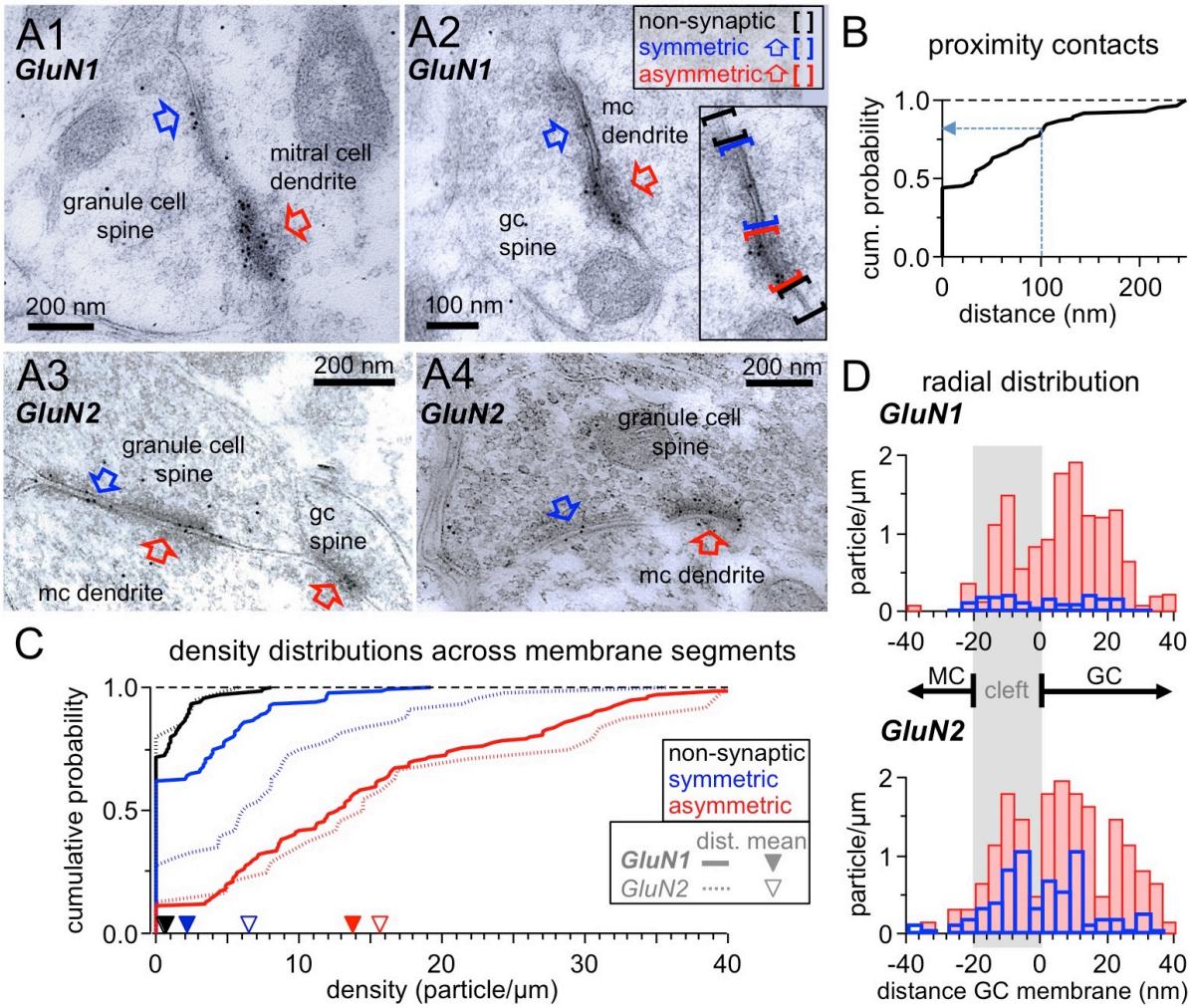

Figure 6. Ultrastructural analysis of the distribution of NMDARs at reciprocal dendro-dendritic synapses.

(**A**) Representative micrographs of reciprocal dendrodendritic synapses labeled for GluN1 (A1 and A2) and GluN2A/B (A3, A4). Note that asymmetric MC-to-GC synapses (red arrows) are strongly labeled and that symmetric GC-to-MC junctions (blue arrows) are also immunopositive. Gold particles are usually not associated with non-synaptic plasma membrane domains of GC spines. The inset in panel A2 illustrates the selection of non-synaptic membrane segments (black brackets), symmetric synapses (blue) and asymmetric synapses (red).

(**B**) Frequency distribution of distances between symmetric and asymmetric synaptic profiles on the same GC spine membrane (based on n = 60 micrographs with both types of profiles on the same spine).

(**C**) Frequency distributions of labeling densities across synaptic (symmetric and asymmetric) and non-synaptic membrane segments for GluN1 (thick lines) and GluN2A/B (thin dotted lines). The arrows on the x-axis indicate the mean density (GluN1: solid, GluN2A/B: open). Color code as in (A).

(**D**) Radial distribution of gold particles representing GluN1 (top panel) and GluN2A/B (bottom panel) at asymmetric (red) and symmetric (blue) synapses. Particle numbers were normalized to the total length of the respective synaptic segments.

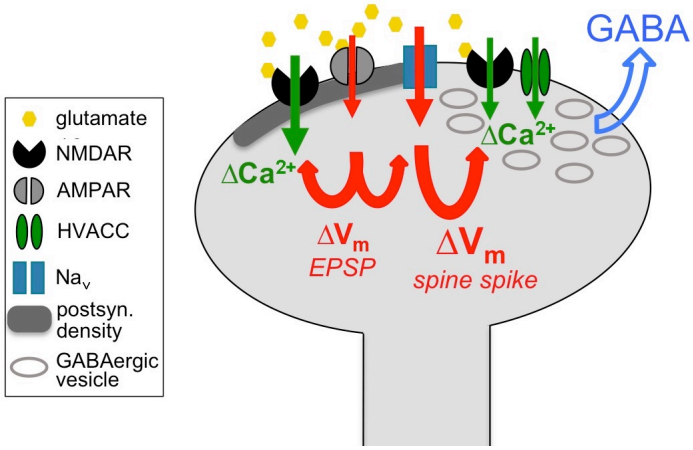

Figure 7 Summary: Mechanisms leading to release of GABA from the granule cell spine. Depolarizing currents are indicated by red arrows and Ca^{2+} entry by green arrows. Upon binding of glutamate, AMPARs get activated, leading to depolarization of the spine, then activation of both post- and presynaptic NMDARs and Na_vs. The latter in turn drive further depolarization, i.e. the spine spike, which both activates HVACCs and enhances Ca^{2+} entry via NMDARs by additional relief of their Mg^{2+} block. HVACC- and presynaptic NMDAR-mediated Ca^{2+} currents cooperate to promote release of GABA.

588 **Methods**

589 *Animal handling, slice preparation and electrophysiology*

590 Animals used in our experiments were juvenile Wistar or VGAT-Venus transgenic rats
591 (VGAT-Venus /w-Tg(SLc32a1-YFP*)1Yyan) of either sex (P11 – P19). VGAT-Venus
592 transgenic rats are based on mouse BAC transgenic lines. They were generated by Drs. Y.
593 Yanagawa, M. Hirabayashi and Y. Kawaguchi at the National Institute for Physiological
594 Sciences, Okazaki, Japan, using pCS2-Venus provided by Dr. A. Miyawaki (Uematsu et al.,
595 2008), RRID: RGD_2314361. In this rat line, fluorescent Venus protein is preferentially
596 expressed in cells carrying the vesicular GABA transporter (VGAT), i.e. GABAergic neurons:
597 the localization of Venus-labeled cells across OB layers was found to be similar to that of
598 GABA-positive cells; direct colocalization in the cortex yielded an overlap of 97% (Uematsu
599 et al., 2008).

600 Sagittal olfactory bulb brain slices (thickness 300 µm) were prepared in ACSF (composition
601 see below) following procedures in accordance with the rules laid down by the EC Council
602 Directive (86/89/ECC) and German animal welfare legislation. Slices were incubated a water
603 bath at 33°C for 30 min and then kept at room temperature (22°C) until recordings were
604 performed.

605 Olfactory bulb mitral cells were visualized by gradient contrast and recorded from in whole
606 cell voltage clamp mode (at -70 mV or +10 mV) or current clamp mode. Recordings were
607 made with an EPC-10 amplifier and Patchmaster v2.60 software (both HEKA Elektronik,
608 Lambrecht/Pfalz, Germany). Experiments were performed at room temperature (22°C).
609 Patch pipette resistance ranged from 5-6-MΩ. Mitral cells clamped at -70 mV were filled with
610 intracellular solution containing the following substances (in mM): (1) tip solution: 130 K-
611 Methylsulfate, 10 HEPES, 4 MgCl2, 2 Ascorbic acid, 10 Phosphocreatine-di-tris-salt, 2.5
612 Na2ATP, 0.4 NaGTP (2) backfilling solution: 110 Cs-Chloride, 10 HEPES, 10 TEA, 4MgCl2,
613 2 Ascorbic acid, 10 5-N-(2,6-dimethylphenylcarbamoylmethyl) triethylammonium bromide
614 (QX-314, Sigma), 0.2 EGTA, 10 Phosphocreatine, 2.5 Na2ATP, 0.4 NaGTP. Mitral cells
615 clamped at + 10 mV contained internal solution composed of: 125 Cs-methanesulfonate 1
616 NaCl, 0.5 EGTA, 10 HEPES, 3 MgATP, 0.3 NaGTP, 10 Phosphocreatine-di-Tris-salt, 10 QX-

617 314, 0.05 Alexa 594 (Ca^{2+} indicator, Thermofisher Scientific, Waltham. Massachusetts, US),
618 at pH 7.3.
619 For current clamp experiments the internal solution contained: 130 K-Methylsulfate, 10
620 HEPES, 4 MgCl2, 2 Ascorbic acid, 10 Phosphocreatine-di-Tris-salt, 2.5 Na2ATP, 0.4
621 NaGTP. Single APs were evoked by somatic current injection (3 ms, 1 nA) and 5 APs were
622 elicited for every recording condition. Cells with leak currents > 200 pA (at V_{hold} = - 70 mV)
623 were discarded. We chose a hyperpolarized holding potential in order to reduce the
624 activation of NMDA autoreceptors on MC lateral dendrites.
625 The extracellular ACSF was bubbled with carbogen and contained (in mM): 125 NaCl, 26
626 $NaHCO_3$, 1.25 NaH_2PO_4, 20 glucose, 2.5 KCl, 1 $MgCl_2$, and 2 $CaCl_2$. The following
627 pharmacological agents were bath-applied in some experiments: bicucculline (BCC, 50 µM,
628 Sigma-Aldrich), ω-conotoxin MVIIC (CTX, 1 µM, Alomone, Jerusalem, Israel), TTX (500 nM,
629 Alomone), D-APV (25 µM, Tocris), gabazine (GBZ, 20 µM, Tocris). In pharmacological
630 experiments we waited for 10 minutes after wash-in of the drugs TTX, APV resp. CTX. In
631 CTX experiments 1mg/ml cyctochrome C was added to the ACSF. TTX voltage clamp
632 experiments were conducted at clamping potentials of -70 mV (n = 5) or + 10 mV (n = 7),
633 whereas all CTX and APV voltage clamp experiments were conducted at + 10 mV.
634 *Combined two-photon imaging and uncaging*
635 Imaging and uncaging were performed on a Femto-2D-uncage microscope (Femtonics,
636 Budapest, Hungary). Two tunable, Verdi-pumped Ti:Sa lasers (Chameleon Ultra I and II
637 respectively, Coherent, Santa Clara, CA, USA) were used in parallel. The first laser was set
638 either to 900 nm for simultaneous excitation of YFP and Alexa 594 in one channel for
639 visualization of spines and the mitral cell for urIPSC recordings, and the second laser was
640 set to 750 nm for uncaging of caged glutamate. The two laser lines were directly coupled into
641 the pathway of the microscope with a polarization cube (PBS102, Thorlabs Inc, Newton, NJ,
642 USA) and two motorized mirrors. As caged compound we used DNI-caged glutamate (DNI;
643 Femtonics). DNI was used in 1 mM concentration in a closed perfusion circuit with a total
644 volume of 12 ml. Caged compounds were washed in for at least 10 minutes before starting
645 measurements. The uncaging laser was switched using an electro-optical modulator

646 (Pockels cell model 350-80, Conoptics, Danbury, CT, USA). The emitted fluorescence was
647 split into a red and a green channel with a dichroic mirror.

648 Triggering of mitral cell reciprocal IPSCs

649 The region of interest on a proximal lateral mitral cell dendrite was moved to the center of the
650 scanning field. In some initial experiments, four uncaging spots were placed in close
651 apposition along the lateral mitral cell dendrite in case of 'blind' uncaging (n = 8 out of total
652 number of successful experiments n = 44). In most experiments, a single uncaging spot was
653 positioned near the region of interest, using YFP fluorescence of GABAergic cells in VGAT-
654 Venus rats as an optical guide to identify potential synaptic contacts between MC lateral
655 dendrites and GC spines.

656 The parameter settings for two-photon uncaging were as established previously on the same
657 experimental rig for precise mimicking of unitary synaptic Ca^{2+} transients in GC spines
658 (Egger et al., 2005; Bywalez et al., 2015). These parameter settings were routinely verified in
659 parallel test experiments, where we imaged Ca^{2+} transients in GC spines following TPU (as
660 in Bywalez et al. 2015). The uncaging power was adjusted to the depth of the measured
661 region of interest, corresponding to a laser power of approximately 15 mW at the uncaging
662 site (Sobczyk et al., 2005). The uncaging beam was positioned at ~ 0.2 - 0.5 µm distance
663 from the MC dendrite/GC spine head. The uncaging pulse duration was 1 ms. The scanning
664 position was readjusted if necessary before each measurement to account for drift. The
665 microscope was equipped with a 60x Nikon Fluor water immersion objective (NA 1.0; Nikon
666 Instruments, Tokyo, Japan). The microscope was controlled by MES v.5.3190 software
667 (Femtonics).

668 *Uncaging stability*

669 To test for the stability of uncaging evoked recurrent IPSCs in MCs, uncaging at a dendritic
670 region of interest was performed. If repeated uncaging led to the apparent occurrence of
671 urIPSCs within the same time window (see below for anlysis details), the stability
672 measurement was continued by either uncaging 30 times in total with a frequency of 0.033
673 Hz (every 30 s) or 5 times in a row with 0.033 Hz followed by a 10 min break (to mimic the
674 time for wash-in of pharmacological compounds) and another round of uncaging (5x,

675 0.033Hz). urIPSC amplitudes were taken from averages of the first 5 – 10 and the last 5 – 10
676 uncaging sweeps and statistically compared with each other.

677 *Electrophysiology: Data analysis and statistics*

678 Electrophysiological data were analysed with custom written macros in Igor pro
679 (Wavemetrics, Lake Oswego, OR, USA). Additional sIPSC and urIPSC analysis was
680 performed using the MiniAnalysis program (Synaptosoft, Decature, GA, USA) and Origin
681 (Northampton, MA, USA).

682 Detection of urISPCs Due to the high spontaneous activity, in order to test for the presence
683 of a signal we performed first an area and event analysis of IPSC traces (see below and Fig.
684 1D; if a signal was detected based on these analyses, we went on to search for individual
685 triggered urIPSCs by visual inspection of an overlay of the recorded traces. Individual IPSCs
686 were considered as uncaging-evoked when they repetitively occurred within the same time
687 window (width 3 ± 2 ms, n = 35) after uncaging and had similar kinetics (indicating a similar
688 location of the respective input on the dendrite). Signal types ranged from single urIPSC
689 events to barrages of urIPSCs lasting tens to hundreds of ms. The release probability was
690 estimated based on 5 – 30 TPU samplings with a mean of 7.5 ± 1.7 stimulations (n = 44).

691 Area analysis The area was measured in individual traces as the integrated activity above
692 baseline for a 500 ms pre-uncaging baseline window and for a 500 ms post-uncaging
693 window, in order to screen for the presence of a signal (Fig. 1D). The 500 ms extent of the
694 time windows was validated by our measurements of averaged barrage duration (see Fig.
695 S1D2).

696 Delta (Δ) area values were calculated by subtracting the area of the 500 ms pre-uncaging
697 baseline window ('pre') from the 500 ms post-uncaging window ('post'), in order to isolate the
698 amount of uncaging-evoked inhibitory activity from spontaneous activity. If this procedure
699 was applied to averaged traces and the result was negative, the Δ_area value was set to
700 zero (i.e. no uncaging-evoked activity). While this procedure might still generate false
701 positives due to spontaneous bursts of activity in the post-uncaging window, it also prevents
702 a spurious cancelling of activity (false negative) that otherwise might happen upon averaging
703 Δ_area across an entire set of experiments. Δ_area values for pharmacological conditions

704 were normalized to control Δ_area in order to assess the net effect of drugs on uncaging-
705 evoked inhibitory activity (Fig. 2D, 3D, 4D).
706 Event analysis Within the individual recorded traces, the peak time points of individual IPSCs
707 were analysed. Peak search parameters in MiniAnalysis were adjusted in order to detect
708 potentially all IPSCs within a trace. For detailed spontaneous IPSC amplitude analysis,
709 IPSCs were sorted manually after the automated peak search and discarded if the amplitude
710 exceeded less than 5 pA and/or the IPSC onset was not be detected properly. Event counts
711 were averaged for the 500 ms pre-uncaging and the 500 ms post-uncaging windows,
712 respectively.
713 Evaluation of effects of pharmacological agents For determining drug effects, the averaged
714 urIPSC amplitudes were scaled down by the ratio of number of responses to total number of
715 trials, both in control and drug condition, in order to account also for changes in release
716 probability. If no single responses/urIPSCs could be detected anymore in the presence of
717 TTX, CTX or APV according to the criteria described above, we measured the mean
718 amplitude of V_m above baseline in the averaged response at the time point of the maximal
719 response amplitude in control condition. If this value was below 0, the response size was set
720 to 0 pA. If the value was larger than 0, we interpreted it as average drug response amplitude
721 including failures and thus did not scale it. This conservative method prevents false
722 negatives due to lacking sensitivity in individual trials in the presence of the drug.
723 Detection of spontaneous activity Spontaneous IPSCs were recorded prior to wash-in of DNI,
724 in the presence of DNI and in the presence of each pharmacological compound. For each
725 condition, data were analysed for a total duration of 20 s of recordings.
726 Analysis of afterhyperpolarizations All stable MC AP recordings within either baseline or drug
727 condition were averaged (n = 5 each). If between the two conditions the holding membrane
728 potential changed by more than 0.3 mV, or the time course (onset of upstroke relative to
729 onset of step depolarization, width) and/or the amplitude of the AP changed by more than
730 15% from their baseline values, the experiment was discarded. If single individual recordings
731 showed such variations, they were not included in the average. For each average, the AHP
732 amplitude was measured as the maximal negative deflection of the membrane potential from
733 the resting membrane potential.

734 *Simulations*

735 The simulations are based on a published compartmental model in NEURON (Aghvami et
736 al., 2019, ModelDB entry 244687). This model uses the 5-state gating model for NMDA
737 receptors (Destexhe et al., 1998), while the HVACC model is adopted from Hemond et al.
738 2008, with adjustments based on own Ca^{2+} current recordings (see Aghvami et al., 2019).
739 For the simulations shown in Fig. 5, there was no exogenous Ca^{2+} buffer included except for
740 panel E where fluorescence transients were simulated in the presence of 100 µM of the
741 Ca^{2+}-sensitive dye OGB-1 in order to emulate the experimental situation from Bywalez et al.
742 2015.

743 As a readout measure for the temporal overlap between I_{Ca_NMDAR} and I_{Ca_HVACC} we first
744 determined the FWHM (full width half maximum) for each current and then the interval within
745 which the two FWHMs overlapped. At this point, we focussed on temporal relationships and
746 did not account for current amplitudes or integrals, since the Ca^{2+} concentration change
747 within the relevant volume cannot be simulated in NEURON and thus spine Ca^{2+} current
748 amplitudes are of limited meaning. We tested for the robustness of this measure
749 against variation of those model parameters that are crucially involved in the generation of
750 the spine spike, i.e. the resistance of the spine neck (R_{neck}), the conductance of AMPA
751 receptors (g_{AMPA}) and the voltage-gated sodium channel conductance (varied in proportion to
752 the potassium channel conductance, $g_{Na/K}$). Their nominal values in the GC model are 1.7
753 GΩ, 2000 pS and 0.5 S/cm^2 respectively. Each was varied between up to 200% of the
754 nominal value and down until no spine spike was generated any more.

755 *Immunogold labeling and electron microscopy*

756 Immunogold labeling was performed on cryosubstituted rat olfactory bulbs (n = 4 animals, 3
757 months old), that had been used previously; for further details on the fixation, embedding and
758 immunogold labeling procedure see (Sassoè-Pognetto and Ottersen, 2000; Sassoè-Pognetto
759 et al., 2003).

760 To maximize detection of the GluN1 subunit, we used a combination of two rabbit antisera as
761 described in Sassoè-Pognetto et al. (2003). One antiserum (kindly donated by Anne
762 Stephenson) binds an extracellular domain (amino acid residues 17–35) common to all splice
763 variants of the GluN1 subunit (Chazot et al., 1995; Racca et al., 2000). The other antiserum

764 was raised against a C-terminal domain and recognizes four splice variants (Chemicon,
765 Temecula, CA; catalog No. AB1516).
766 For GluN2, we used a affinity-purified rabbit antibody raised against a synthetic peptide
767 corresponding to the C-terminus of the GluN2A subunit conjugated to BSA (Chemicon, cat.
768 no. AB1548). According to the manufacturer, this antibody recognizes the GluN2A and
769 GluN2B subunits in Western blot analysis of transfected cells.
770 *Ultrastructure data analysis and statistics*
771 Grid squares were analysed systematically for the presence of synaptic profiles (symmetric
772 and/or asymmetric) between GC spines and MC dendrites (Fig. 6; see also Fig. 1A in
773 Sassoè-Pognetto and Ottersen, 2000). Synaptic profiles were then photographed at high
774 magnification (75.000 - 120.000x) with a side-mounted CCD camera (Mega View III,
775 Olympus Soft Imaging System). The plasma membrane of GC spines, when clearly visible,
776 was classified as either belonging to an asymmetric synaptic profile, a symmetric profile, or a
777 non-synaptic segment (see Fig. 6A2 for examples). The length of segments was measured
778 along the spine membrane curvature (using ImageJ 1.52 analysis software) and the number
779 of immunogold particles within a distance of ≤ 30 nm from the GC spine membrane was
780 counted for the individual segments. The lengths of non-synaptic segments were on average
781 longer than those of synaptic segments, which argues against an undersampling of gold
782 particle densities in non-synaptic membranes compared to synaptic membranes and thus a
783 false positive difference between the density distribution in non-synaptic membranes and
784 symmetric profiles (GluN1: mean non-synaptic segment length: 610 ± 400 nm, n = 138,
785 symmetric synaptic profiles: 270 ± 120 nm, n = 120, asymmetric synaptic profiles: 260 ± 110
786 nm, n = 111; similar results for GluN2, not shown). When both symmetric and asymmetric
787 synaptic profiles were visible in the same individual spine, the distance of such reciprocal
788 contacts was also measured along the curvature of the GC spine membrane.
789 The distribution of labeling along the axis perpendicular to the GC spine membrane (radial
790 axis) was determined by examining micrographs of transversely cut synaptic profiles, with
791 well defined presynaptic and postsynaptic membranes. Here all particles at distances up to
792 40 µm were counted to prevent a possible bias.
793 *Statistical tests*

794 All electrophysiological data were analysed with non-parametric paired (*Wilcoxon matched*
795 pairs) or unpaired (*Mann-Whitney-U*) tests and expressed as mean ± SD. The density
796 distributions of immunogold particles were compared with the Kolmogorov-Smirnov test
797 (https://www.wessa.net/rwasp_Reddy-Moores%20K-S%20Test.wasp).
798

799 ***Author contributions***

800 VLR performed all uncaging experiments. LZ performed MC current clamp recordings. VLR,
801 GB, MSP and VE analyzed data. SSA performed simulations. VE and VLR designed
802 research and wrote the manuscript, with MSP contributing to the parts on ultrastructure. BR
803 provided DNI-caged glutamate and assisted in editing the manuscript.

804 ***Acknowledgments***

805 We thank Anne Pietryga-Krieger for expert technical assistance, Marius Stephan and Philipp
806 Seidel for assistance with IPSC analysis, Gagik Yeghiazaryan for initial MC current clamp
807 recordings, Imre Vida for facilitating access to VGAT-Venus rats, and Sigrun Korsching and
808 Yoshiyuki Kubota for advice on statistics. This work was funded mainly by the German
809 Federal Ministry for Education and Research (BMBF, 01GQ1104/01GQ1502), with additional
810 equipment funding by LMU-GSN, DFG-SFB 870 and funding for staff from GIF (1479-418.13;
811 all to VE), and by ERC 682426, GINOP_2.1.1-15-2016-00979, VKSZ_14-1-2015-0155,
812 712821-NEURAM to BR.

813 ***Competing interests***

814 There are competing financial interests since BR is a founder of Femtonics Kft and a
815 member of its scientific advisory board. No other competing interests exist.

816 ***References***

817 1. Abraham, N. M., Egger, V., Shimshek, D. R., Renden, R., Fukunaga, I., Sprengel, R.,
818 Seeburg, P. H., Klugmann, M., Margrie, T. W., Schaefer, A. T., & Kuner, T. (2010). Synaptic
819 inhibition in the olfactory bulb accelerates odor discrimination in mice. *Neuron, 65*(3), 399-
820 411.
821 2. Aghvami, S., Müller, M., Araabi ,B.N., & Egger V. (2019) Coincidence detection within the
822 excitable rat olfactory bulb granule cell spines. *J. Neurosci*. 39, 584-595. doi:
823 10.1523/JNEUROSCI.1798-18.2018
824 3. Angelo, K., & Margrie, T. W. (2011). Population diversity and function of hyperpolarization-
825 activated current in olfactory bulb mitral cells. *Sci Rep, 1*, 50. doi:10.1038/srep00050

4. Arnson, H. A., & Strowbridge, B. (2017). Spatial Structure Of Synchronized Inhibition In The Olfactory Bulb. *J Neurosci,* 37(43):10468 –10480. doi:10.1523/JNEUROSCI.1004-17.2017
5. Aroniadou-Anderjaska, V., Ennis, M., & Shipley, M. T. (1999). Dendrodendritic recurrent excitation in mitral cells of the rat olfactory bulb. *J Neurophysiol, 82*(1), 489-494. doi:10.1152/jn.1999.82.1.489
6. Banerjee, A., Larsen, R.S., Philpot, B.D., & Paulsen,O. (2016). Roles of Presyanptic NMDA Receptors in Neurotransmission and Plasticity. *Trends in Neurosciences* 39 (1). http://dx.doi.org/10.1016/j.tins.2015.11.001
7. Bartel, D. L., Rela, L., Hsieh, L., & Greer, C. A. (2015). Dendrodendritic synapses in the mouse olfactory bulb external plexiform layer. *J Comp Neurol, 523*(8), 1145-1161. doi:10.1002/cne.23714
8. Bloodgood, B. L., & Sabatini, B. L. (2007). Ca(2+) signaling in dendritic spines. *Curr Opin Neurobiol, 17*(3), 345-351. doi:10.1016/j.conb.2007.04.003
9. Bouvier, G., Bidoret, C., Casado, M., & Paoletti, P. (2015). Presynaptic NMDA receptors: Roles and rules. *Neuroscience, 311*, 322-340. doi:10.1016/j.neuroscience.2015.10.033
10. Bywalez, W. G., Patirniche, D., Rupprecht, V., Stemmler, M., Herz, A. V. M., Pálfi, D., Rozsa, B., & Egger, V. (2015). Local Postsynaptic Voltage-Gated Sodium Channel Activation in Dendritic Spines of Olfactory Bulb Granule Cells. *Neuron, 85*(3), 590-601. doi:10.1016/j.neuron.2014.12.051
11. Carlson, G. C., Shipley, M. T., & Keller, A. (2000). Long-lasting depolarizations in mitral cells of the rat olfactory bulb. *J Neurosci, 20*(5), 2011-2021.
12. Chazot, P.L., Cik, M., & Stephenson, F.A. (1995) An investigation into the role of N-glycosylation in the functional expression of a recombinant heteromeric NMDA receptor. Mol Membr Biol, 12(4):331-337.
13. Chen, W. R., Xiong, W., & Shepherd, G. M. (2000). Analysis of relations between NMDA receptors and GABA release at olfactory bulb reciprocal synapses. *Neuron, 25*(3), 625-633.
14. Chiovini, B., Turi, G. F., Katona, G., Kaszas, A., Palfi, D., Maak, P., Szalay, G., Szabo, M. F., Szabo, G., Szadai, Z., Kali, S., & Rozsa, B. (2014). Dendritic spikes induce ripples in parvalbumin interneurons during hippocampal sharp waves. *Neuron, 82*(4), 908-924. doi:10.1016/j.neuron.2014.04.004
15. Crespo, C., Liberia, T., Blasco-Ibáñez, J.M., Nácher, J., & Varea, E. (2013). The circuits of the olfactory bulb. The exception as a rule. Anat Rec (Hoboken)., 296(9):1401-1412. doi: 10.1002/ar.22732.
16. Destexhe, A., Mainen, Z.F., & Sejnowski, T.J. (1998). Kinetic models of synaptic transmission. In: Methods in Neuronal Modeling (2nd edition; edited by Koch, C., & Segev, I.). MIT press, Cambridge, 1998, 1-25.
17. Didier, A., Carleton, A., Bjaalie, J. G., Vincent, J. D., Ottersen, O. P., Storm-Mathisen, J., & Lledo, P. M. (2001). A dendrodendritic reciprocal synapse provides a recurrent excitatory connection in the olfactory bulb. *Proc Natl Acad Sci U S A, 98*(11), 6441-6446.

865 18. Duguid, I., & Smart, T.G. (2004) Retograde activation of presynaptic NMDA receptors
866 enhances GABA release at cerebellar interneuton-Purkinje cell synapses. *Nat Neurosci*, 7(5),
867 525-533.
868 19. Duménieu, M., Fourcaud-Trocmé, N., Garcia, S., & Kuczewski, N. (2015).
869 Afterhyperpolarization (AHP) regulates the frequency and timing of action potentials in the
870 mitral cells of the olfactory bulb: role of olfactory experience. Physiol Rep, 3(5). pii: e12344.
871 doi: 10.14814/phy2.12344.
872 20. Egger, V. (2008). Synaptic sodium spikes trigger long-lasting depolarizations and slow
873 calcium entry in rat olfactory bulb granule cells. *Eur J Neurosci, 27*(8), 2066-2075.
874 21. Egger, V., Svoboda, K., & Mainen, Z. F. (2005). Dendrodendritic synaptic signals in olfactory
875 bulb granule cells: Local spine boost and global low-threshold spike. *J Neurosci, 25*, 3521-
876 3530.
877 22. Egger, V., & Urban, N. N. (2006). Dynamic connectivity in the mitral cell-granule cell
878 microcircuit. *Semin Cell Dev Biol, 17*(4), 424-432.
879 23. Friedman, D., & Strowbridge, B. W. (2000). Functional role of NMDA autoreceptors in
880 olfactory mitral cells. *J Neurophysiol, 84*(1), 39-50. doi:10.1152/jn.2000.84.1.39
881 24. Fukunaga, I., Herb, J. T., Kollo, M., Boyden, E. S., & Schaefer, A. T. (2014). Independent
882 control of gamma and theta activity by distinct interneuron networks in the olfactory bulb. *Nat*
883 *Neurosci, 17*(9), 1208-1216. doi:10.1038/nn.3760
884 25. Gilra, A., & Bhalla, U. S. (2015). Bulbar Microcircuit Model Predicts Connectivity and Roles of
885 Interneurons in Odor Coding. *PLoS ONE, 10*(5), e0098045.
886 doi:10.1371/journal.pone.0098045
887 26. Glitsch, M., & Marty, A. (1999). Presynaptic Effects of NMDA in Cerebellar Purkinje Cells and
888 Interneurons. J Neurosci, 19(2):511-519.
889 27. Grunditz, Å., Holbro, N., Tian, L., Zuo, Y., & Oertner, T.G. (2008). Spine Neck
890 Plasticity Controls Postsynaptic Calcium Signals through Electrical
891 Compartmentalization. J Neurosci 28:13457-13466.
892 28. Halabisky, B., Friedman, D., Radojicic, M., & Strowbridge, B. W. (2000). Calcium influx
893 through NMDA receptors directly evokes GABA release in olfactory bulb granule cells. *J*
894 *Neurosci, 20*(13), 5124-5134.
895 29. Hemond, P., Epstein, D., Boley, A., Migliore, M., Ascoli, G.A., & Jaffe, D.B. (2008).
896 Distinct classes of pyramidal cells exhibit mutually exclusive firing patterns in
897 hippocampal area CA3b. *Hippocampus* 18:411-424.
898 30. Huang, L., Garcia, I., Jen, H.-I., & Arenkiel, B. R. (2013). Reciprocal connectivity between
899 mitral cells and external plexiform layer interneurons in the mouse olfactory bulb. *Frontiers in*
900 *Neural Circuits, 7*. doi:10.3389/fncir.2013.00032
901 31. Isaacson, J. S. (1999). Glutamate spillover mediates excitatory transmission in the rat
902 olfactory bulb. *Neuron, 23*(2), 377-384.
903 32. Isaacson, J. S. (2001). Mechanisms governing dendritic gamma-aminobutyric acid (GABA)

904 release in the rat olfactory bulb. *Proc Natl Acad Sci U S A, 98*(1), 337-342.
905 33. Isaacson, J. S., & Strowbridge, B. W. (1998). Olfactory reciprocal synapses: dendritic
906 signaling in the CNS. *Neuron, 20*(4), 749-761.
907 34. Kaeser, P. S., & Regehr, W. G. (2014). Molecular mechanisms for synchronous,
908 asynchronous, and spontaneous neurotransmitter release. *Annu Rev Physiol, 76*, 333-363.
909 doi:10.1146/annurev-physiol-021113-170338
910 35. Kampa, B., Clements, J., Jonas, P., & Stuart, G.J. (2004) Kinetics of Mg2+ unblock of NMDA
911 receptors: implications for spike-timing dependent synaptic plasticity. J Physio, 556.2, 337-
912 345.
913 36. Kapoor, V., & Urban, N. N. (2006). Glomerulus-specific, long-latency activity in the olfactory
914 bulb granule cell network. *J Neurosci, 26*, 11706-11719.
915 37. Kato, H. K., Gillet, S. N., Peters, A. J., Isaacson, J. S., & Komiyama, T. (2013). Parvalbumin-
916 expressing interneurons linearly control olfactory bulb output. *Neuron, 80*(5),
917 10.1016/j.neuron.2013.1008.1036. doi:10.1016/j.neuron.2013.08.036
918 38. Kay, L. M. (2003). Two species of gamma oscillations in the olfactory bulb: dependence on
919 behavioral state and synaptic interactions. *J Integr Neurosci, 2*(1), 31-44.
920 39. Khawaled, R., Bruening-Wright, A., Adelman, J. P., & Maylie, J. (1999). Bicuculline Block of
921 Small-conductance Calcium-activated Potassium Channels. *Pflügers Archiv : Eur J Physiol.*
922 **438** (3): 314–321. doi:10.1007/s004240050915.
923 40. Lagier, S., Carleton, A., & Lledo, P.-M. (2004). Interplay between Local GABAergic
924 Interneurons and Relay Neurons Generates Gamma Oscillations in the Rat Olfactory Bulb. *J*
925 *Neurosci*, 24(18):4382– 4392.
926 41. Lepousez, G., Csaba, Z., Bernard, V., Loudes, C., Videau, C., Lacombe, J., Epelbaum, J., &
927 Viollet, C. (2010). Somatostatin interneurons delineate the inner part of the external plexiform
928 layer in the mouse main olfactory bulb. *J Comp Neurol, 518*(11), 1976-1994.
929 doi:10.1002/cne.22317
930 42. Lester, R.A., Clements, J.D.,Westbrook, G.L., & Jahr, C.E. (1990) NMDAR Channel kinetics
931 determine the time course of NMDA receptor-mediated synaptic currents. Nature,
932 346(6284):565-567.
933 43. Lowe, G. (2002). Inhibition of backpropagating action potentials in mitral cell secondary
934 dendrites. *J Neurophysiol, 88*(1), 64-85.
935 44. McGuinness, L., Taylor, C., Taylor, R.D., Yau, C., Langenhan, T., Hart, M.L., Christian, H.,
936 Tynan, P.W., Donnelly, P., & Emptage, N.J. (2010). Presynaptic NMDARs in the
937 hippocampus facilitate transmitter release at theta frequency. *Neuron*, 68(6):1109-1127. doi:
938 10.1016/j.neuron.2010.11.023.
939 45. McIntyre, A. B. R., & Cleland, T. A. (2016). Biophysical constraints on lateral inhibition in the
940 olfactory bulb. *Journal of Neurophysiology, 115*(6), 2937-2949. doi:10.1152/jn.00671.2015
941 46. Miller, J. P., Rall, W., & Rinzel, J. (1985). Synaptic amplification by active membrane in
942 dendritic spines. *Brain Res, 325*(1-2), 325-330.

47. Miyamichi, K., Shlomai-Fuchs, Y., Shu, M., Weissbourd, B. C., Luo, L., & Mizrahi, A. (2013). Dissecting Local Circuits: Parvalbumin Interneurons Underlie Broad Feedback Control of Olfactory Bulb Output. *Neuron, 80*(5), 1232-1245. doi:10.1016/j.neuron.2013.08.027
48. Naritsuka, H., Sakai, K., Hashikawa, T., Mori, K., & Yamaguchi, M. (2009). Perisomatic-targetign Granule Cells in the Mouse Olfactory Bulb. *J Comp Neurol*, 525, 409-426.
49. Nunes, D., & Kuner, T. (2018). Axonal sodium channel NaV1.2 drives granule cell dendritic GABA release and rapid odor discrimination. *PLoS Biol, 16*(8), e2003816. doi:10.1371/journal.pbio.2003816
50. Pálfi, D., Chiovini, B., Szalay, G., Kaszás, A., Turi, G.F., Katona, G., Ábrányi-Balogh, P., Szőri, M., Potor, A., Frigyesi, O., Lukácsné Haveland, C., Szadai, Z., Madarász, M., Vasanits-Zsigrai, A., Molnár-Perl, I., Viskolcz, B., Csizmadia, I.G., Mucsi, Z., & Rózsa, B. (2018). High efficiency two-photon uncaging coupled by the correction of spontaneous hydrolysis. Org Biomol Chem. 16(11):1958-1970. doi: 10.1039/c8ob00025e.
51. Pressler, R. T., & Strowbridge, B. W. (2017). Direct Recording of Dendrodendritic Excitation in the Olfactory Bulb: Divergent Properties of Local and External Glutamatergic Inputs Govern Synaptic Integration in Granule Cells. *J Neurosci, 37*(49), 11774-11788. doi:10.1523/JNEUROSCI.2033-17.2017
52. Racca, C., Stephenson, F.A., Streit, P., Roberts, J.D., & Somogyi, P. (2000). NMDA receptor content of synapses in stratum radiatum of the hippocampal CA1 area. J Neurosci. 20(7):2512-2522.
53. Rannals, M. D., & Kapur, J. (2011). Homeostatic strengthening of inhibitory synapses is mediated by the accumulation of GABA(A) receptors. *J Neurosci, 31*(48), 17701-17712. doi:10.1523/JNEUROSCI.4476-11.2011
54. Sailor, Kurt A., Valley, Matthew T., Wiechert, Martin T., Riecke, H., Sun, Gerald J., Adams, W., . . . Lledo, P.-M. (2016). Persistent Structural Plasticity Optimizes Sensory Information Processing in the Olfactory Bulb. *Neuron, 91*(2), 384-396. doi:http://dx.doi.org/10.1016/j.neuron.2016.06.004
55. Salin, P. A., Lledo, P. M., Vincent, J. D., & Charpak, S. (2001). Dendritic glutamate autoreceptors modulate signal processing in rat mitral cells. *J Neurophysiol, 85*(3), 1275-1282.
56. Sassoé-Pognetto, M., & Ottersen, O. P. (2000). Organization of Ionotropic Glutamate Receptors at Dendrodendritic Synapses in the Rat Olfactory Bulb. J Neurosci, 20(6):2192–2201.
57. Sassoé-Pognetto, M., Utvik, J. K., Camoletto, P., Watanabe, M., Stephenson, F. A., Bredt, D. S., & Ottersen, O. P. (2003). Organization of postsynaptic density proteins and glutamate receptors in axodendritic and dendrodendritic synapses of the rat olfactory bulb. *J Comp Neurol, 463*(3), 237-248.
58. Schmidt, L. J., & Strowbridge, B. W. (2014). Modulation of olfactory bulb network activity by serotonin: synchronous inhibition of mitral cells mediated by spatially localized GABAergic

982 microcircuits. *Learn Mem, 21*(8), 406-416. doi:10.1101/lm.035659.114
983 59. Schoppa, N. E., Kinzie, J. M., Sahara, Y., Segerson, T. P., & Westbrook, G. L. (1998).
984 Dendrodendritic inhibition in the olfactory bulb is driven by NMDA receptors. *J Neurosci,*
985 *18*(17), 6790-6802.
986 60. Sobczyk, A., Scheuss, V., & Svoboda, K. (2005). NMDA receptor subunit-dependent [Ca2+]
987 signaling in individual hippocampal dendritic spines. *J Neurosci, 25*(26), 6037-6046.
988 doi:10.1523/JNEUROSCI.1221-05.2005
989 61. Spruston, N. (2008). Pyramidal neurons: dendritic structure and synaptic integration. *Nat Rev*
990 *Neurosci, 9*(3), 206-221. doi:10.1038/nrn2286
991 62. Stanley, E. F. (2016) The Nanophysiology of Fast Transmitter Release. *Trends Neurosci*. 39
992 (3). http://dx.doi.org/10.1016/j.tins.2016.01.005
993 63. Toida, K., Kosaka, K., Heizmann, C. W., & Kosaka, T. (1994). Synaptic contacts between
994 mitral/tufted cells and GABAergic neurons containing calcium-binding protein parvalbumin in
995 the rat olfactory bulb, with special reference to reciprocal synapses between them. *Brain Res,*
996 *650*(2), 347-352.
997 64. Tonnesen, J., & Nagerl, U. V. (2016) Dendritic Spines as Tunable Regulators of Synaptic
998 Signals. *Front Psychiatry* 7:101. doi: 10.3389/fpsyt.2016.00101
999 65. Uematsu, M., Hirai, Y., Karube, F., Ebihara, S., Kato, M., Abe, K., . . . Kawaguchi, Y. (2008).
1000 Quantitative Chemical Composition of Cortical GABAergic Neurons Revealed in Transgenic
1001 Venus-Expressing Rats. *Cerebral Cortex, 18*(2), 315-330. doi:10.1093/cercor/bhm056
1002 66. Veruki, M. L., Zhou, Y., Castilho, A., Morgans, C. W., & Hartveit, E. (2019) Extrasynaptic
1003 NMDA Receptors on Rod Pathway Amacrine Cells: Molecular Composition, Activation, and
1004 Signaling. *J Neurosci* 39: 627-650. Doi: 10.1523/JNEUROSCI.2267-18.2018
1005 67. Wallace, J. L., Wienisch, M., & Murthy, V. N. (2017). Development and Refinement of
1006 Functional Properties of Adult-Born Neurons. *Neuron, 96*(4), 883-896.e887.
1007 doi:10.1016/j.neuron.2017.09.039
1008 68. Wellis, D. P., & Kauer, J. S. (1993). GABAA and glutamate receptor involvement in
1009 dendrodendritic synaptic interactions from salamander olfactory bulb. *J Physiol, 469*, 315-
1010 339.
1011 69. Wienisch, M., & Murthy, V. N. (2016). Population imaging at subcellular resolution supports
1012 specific and local inhibition by granule cells in the olfactory bulb. *Scientific Reports, 6*, 29308.
1013 doi:10.1038/srep29308
1014 70. Woolf, T. B., Shepherd, G. M., & Greer, C. A. (1991). Serial reconstructions of granule cell
1015 spines in the mammalian olfactory bulb. *Synapse, 7*(3), 181-192.
1016 71. Xiong, W., & Chen, W. R. (2002). Dynamic gating of spike propagation in the mitral cell
1017 lateral dendrites. *Neuron, 34*(1), 115-126.
1018 72. Zhang, L., Huang, Y., & Hu, B. (2016). Olfactory experiences dynamically regulate plasticity
1019 of dendritic spines in granule cells of Xenopus tadpoles in vivo. *Scientific Reports, 6*, 35009.
1020 doi:10.1038/srep35009